Contents lists available at ScienceDirect

Chinese Journal of Aeronautics

Journal homepage: www.elsevier.com/locate/cja

Final Accepted Version

Integral precession calibration method of PIGA on linear vibration table

Chuang SUN[a], Shun-qing REN[b], Jun-wei CAO[c,*], Ru HUO[d]

[a]*Department of Automation, Tsinghua University, Beijing 100080, China*
[b]*School of Astronautics, Harbin Institute of Technology, Harbin 150001, China*
[c]*Beijing National Research Center for Information Science and Technology, Tsinghua University, Beijing 100080, China*
[d]*Faculty of Information technology, Beijing University of Technology, Beijing 100124, China*

Received 24 February 2023; revised July 03 2023; accepted July 23 2023

Abstract

Linear vibration table can provide harmonic accelerations to excite the nonlinear error terms of Pendulous Integrating Gyro Accelerometer (PIGA). Integral precession calibration method is proposed to calibrate PIGA on a linear vibration table in this paper. Based on the precise expressions of PIGA's inputs, the error calibration model of PIGA is established. Precession angular velocity errors of PIGA are suppressed by integer periodic precession and the errors caused by non-integer periods vibrating are compensated. The complete calibration process, including planning, preparation, PIGA testing, and coefficient identification, is designed to optimize the test operations and evaluate the calibration results. The effect of the main errors on calibration uncertainty is analyzed and the relative sensitivity function is proposed to further optimize the test positions. Experimental and simulation results verify that the proposed 10-position calibration method can improve calibration uncertainties after compensating for the related errors. The order of calibration uncertainties of the second- and third-order coefficients are decreased to 10^{-8} rad/s/g^2 and 10^{-8} rad/s/g^3, respectively. Compared with the other two classical calibration methods, the calibration uncertainties of PIGA's nonlinear error coefficients can be effectively reduced and the proportional residual errors are decreased less than 3×10^{-6} rad/s/g by using the proposed calibration method.

Keywords: PIGA; Linear vibration table; Vibration measurement; Calibration; Error analysis; Uncertainty analysis

*Corresponding author. *E-mail address:* jcao@tsinghua.edu.cn

1. Introduction

Nowadays, accelerometers such as quartz accelerometers and Pendulous Integrating Gyro Accelerometers (PIGA) play a vital role which can provide high-precision measurement of acceleration in Inertial Navigation Systems (INS), [1] automotive safety system, [2] and biomedical measurement. [3] With increasing requirements for accuracy and stability, the key to accuracy improvement is advanced calibration methods that can accurately identify the error coefficients of accelerometers.

The general calibration approaches of accelerometers are utilizing multi-axis turntable and centrifuge. Since the local gravitational acceleration and the turn rate of the Earth can be accurately measured, the static multi-position

methods were proposed to calibrate bias and scale factor of accelerometers and gyroscopes.[4,5] Dynamic calibration method was provided to separate the cross-coupling coefficients of a linear accelerometer by utilizing the tilted rotating rate table.[6] The high-g test environment could be typically constructed via precision centrifuges to effectively excite the high-order error coefficients. The 12-position methods were adopted to calibrate the nonlinear coefficients by compensating for static radius errors via a low-cost centrifuge.[7] The double turntable centrifuge was developed to suppress the installation errors and reduce the test costs.[8] The high-order error terms of accelerometers and gyroscopes were calibrated by dynamic centrifuges, which can provide constant centripetal and harmonic acceleration.[9-11]

Compared with the centrifuge, the simpler vibration tables can simulate the vibration environment, measure the sensitivity to dynamic accelerations, and calibrate the nonlinear error coefficients of accelerometers with a lower cost.[12-15] In addition, due to the smaller angle motion of the linear vibration table, it is suitable for calibrating the coefficients of gyroscope and PIGA.[14,16] The existing literatures have been surveyed and analyzed from the following aspects as shown in Table 1[14,17-22]: calibration objects, error analysis of calibration systems, error compensation, calibration method, test mode, optimal design of process, and calibration magnitude or resolution. The calibration method of integer periodic precession was proposed to improve the output accuracy of PIGA.[15] Some works presented the vibration measurement method of the accelerometer's Vibration Rectification Error (VRE) and transverse sensitivity.[17,18] Some authors proposed a 6-directional method for calibrating the nonlinear error coefficients of quartz accelerometer.[19] The installation errors were compensated by integrating the static state test and random vibration test.[20] He et al.[21] proposed the separation method of nonlinear quadratic term of PIGA within integer periods vibration. Ren and Sun[22] proposed the integer periodic vibration method for calibrating the high-order error coefficients of PIGA.

Table 1 Summary of existing calibration methods.

Ref.	Object	Error Analysis	Error Compensation	Calibration Method	Test Mode	Optimal Design	Magnitude (ppm)	Remark
[14]	Second-order	Harmonic distortion	×	Integer periodic vibration	6-position	×	1	A calibration method of gyroscope
[17]	VRE	Pendulum deflection	×	Fixed-frequency vibration	×	×	1000	An analysis method of VRE
[18]	Transverse sensitivity	×	×	*Simulation*	4-frequency	×	1	A simulation of transverse sensitivity
[19]	High-order	×	×	Fixed-timing vibration	6-direction	×	10	A calibration method of quartz accelerometer
[20]	Second-order	Installation error	✓	1-6g random vibration	Multi-frequency	×	10	A calibration method of accelerometers
[21]	Second-order	×	×	Integer periodic precession	Multi-frequency	×	100	A calibration method of PIGA
[22]	High-order	Main error sources	✓	Integer periodic vibration	Multi-frequency & 6-position	×	1-10	A calibration method of PIGA
Our	**High-order**	**Main error sources**	✓	**Integer periodic precession & vibration**	**Multi-frequency & multi-position**	✓	**1**	**A calibration method of PIGA**

NOTE: The abbreviation ppm means parts per million.

Summarily, most of the aforementioned references present the multi-position and multi-frequency test mode for calibrating the second-order error coefficients of accelerometers without considering the error propagation analysis and error compensation.[14-19] Furthermore, the design of parameters and process of calibration test were not optimized in these references to further improve the calibration effectiveness and efficiency. For the high-precision accelerometer, the calibration method of integer periodic vibration can reduce the influence of measurement errors on the accuracy of output accelerations,[14,17,22] and the integer periodic precession can improve the output accuracy of PIGA.[15,21] However, the closure errors caused by non-integer periodic vibration are not considered.

Consequently, the integer periodic precession methods and the integer periodic vibration methods are separately applied into the existing calibration schemes, which means that the measurement accuracy of calibration objects and test equipment cannot be improved simultaneously. In this paper, an optimal and integral calibration method for PIGA precession within integer periods on a linear vibration table is proposed. The error calibration model of PIGA precession within integer periods is established based on the calculated inputs and the working principle of PIGA. Then, the detailed calibration process is optimized based on the D-optimal design and uncertainty estimation. Thus, the main nonlinear error coefficients of PIGA can be accurately and efficiently calibrated. The main contributions of this paper are presented as follows.

(1) The measurement uncertainty of PIGA can be improved by the proposed integral precession calibration method. In addition, the influence of vibration errors can be significantly restrained by compensating for the corresponding inputs from integer periodic vibration.

(2) The sensitivity analyses are proposed to precisely evaluate the effect on the calibration uncertainty and the va-

lidity of the optimum design test positions.

(3) The comprehensive analyses of calibration results are proposed. The optimized test process of PIGA calibration is arranged and the proportional residual error is designed to enhance the efficiency of the calibration test.

The remainder of this article is organized as follows. In Section 2, the corresponding coordinate systems of the calibration system are established. Then, the precise inputs of PIGA are deduced in Section 3. In Section 4, the error calibration model of PIGA precession within integer periods is proposed. The calibration process is designed in three parts, including planning and preparation, PIGA testing, and coefficient identification in Section 5. The experiments and simulations are constructed to verify the effectiveness of the proposed calibration method in Section 6. The conclusions are drawn in Section 7.

2. Calibration system

The calibration system is shown in Fig.1. The system consists of a precision linear vibration table, indexing head, control & monitoring system, and PIGA. The linear vibration table consists mainly of a crank disk, center bearing, end bearing, read head, grating scale, and table top. The distance between the center point of the center bearing and the center point of the end bearing is denoted as A_0 (A_0 = 0.03 m). The read head and grating scale are used to measure the displacement of the table top. The grating scale is Renishaw RELA absolute linear grating, of which the accuracy is better than ± 1 μm in the distance of 1 m. In addition, TONiC grating system is used for frequency measurement and monitor, which is composed of a Renishaw T1000-10A reading head and an RGSZ grating ruler. Ideally, when the center bearing is driven by the brush-less DC torque motor with the constant angular velocity $-\omega_v$ (rad/s), the end bearing will horizontally reciprocate with the horizontal guide rail constraint. Then, the table top will vertically reciprocate with the vertical guide rail constraint. Thus, at time t, the displacement of the table top is $-A_0\sin\omega_v t$ and the output acceleration is $A_0\omega_v^2\sin\omega_v t$ in the vertical direction. The indexing head is installed on the table top to modify the test poses of PIGA. Then PIGA is mounted on the indexing head as shown in Fig.1. The control & monitoring system is used to control the measurement system which includes servo circuit, output circuit, magnetic suspension circuit, temperature control circuit, etc. The software operation interface includes parameter setting, device status information, process information, measurement information, and result information for monitoring the real-time running status. The power module provides 45 kW power and the data sampling module includes data processing software and industrial computer.

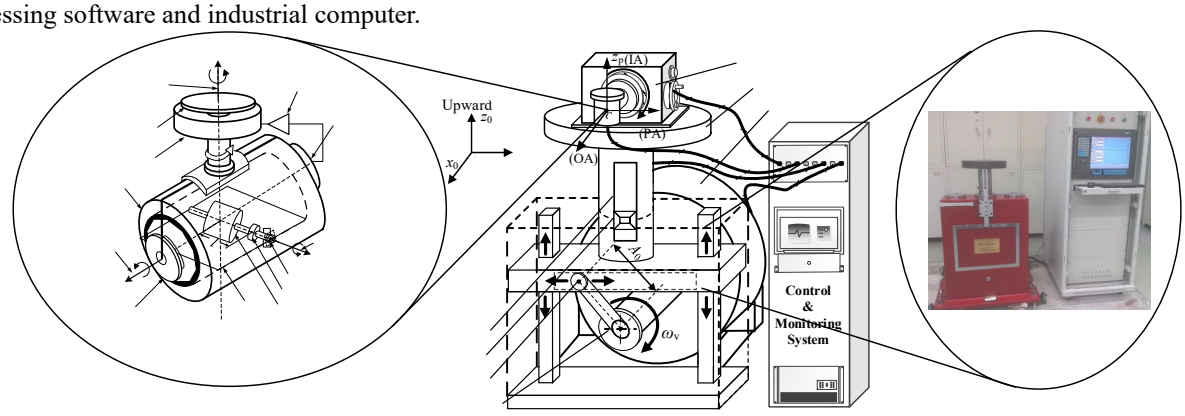

Fig. 1 Schematic diagram of calibration system.

The PIGA comprises a single-axis float gyroscope, spin motor pendulous mass, electromagnetic signal generator, cylindrical shell, torque motor, signal amplifier, temperature sensor, and cylindrical housing, as shown in Fig.1. The float gyroscope with the pendulous mass m is unbalanced located on its Pendulous Axis (PA) line, of which the displacement between the center of the gyro rotor's mass and the pendulous mass is l. The acceleration a_I in the Input Axis (IA) direction causes motion about the output axis Then, the corresponding torque mla_I about the Output Axis (OA) causes relative rotation of the cylindrical shell. The cylindrical shell will precess about the IA axis while the output unit measures the precession angular velocity $\dot{\alpha}$ by counting the output pulse. When the gyroscope's angular momentum is H_A, a reaction torque $H_A\dot{\alpha}$ is present due to the friction torque and other disturbance torques. The concentric cylindrical housing will rotate about the OA axis with the angular velocity β. The torque motor generates the balancing torque to offset the interference torque caused by the precession of the OA axis. The electromagnetic signal generator is used to measure the rotation of the float gyroscope with respect to the cylindrical shell and the signal amplifier is used to amplify the signal. Thus, $\dot{\beta}\approx 0$, $\ddot{\beta}\approx 0$, and the kinetic equation of PIGA is:

$$\ddot{\alpha}=\frac{ml a_{\mathrm{l}}-M_{\mathrm{y}}\ddot{\beta}-C_{\mathrm{m}}\dot{\beta}}{H_{\mathrm{A}}}\approx\frac{ml}{H_{\mathrm{A}}}a_{\mathrm{l}} \tag{1}$$

where M_{y} is the rotational inertia of the inner frame of the gyroscope and C_{m} is the damping coefficient.

Generally, Euler angles are applied to describe the motions of inertial test equipment and inertial navigation system.[22,23] According to the operating principle of the linear vibration table, the coordinate systems are established based on the Euler transform, as shown in Fig.2. Then, the corresponding parameters and expressions are shown in Table 2.

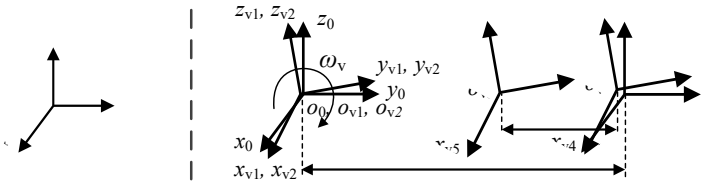

Fig. 2 Main coordinate systems of measurement system.

Table 2 Coordinate systems and main parameters of measurement system.

Coordinate system	Main parameter	Value	H -matrix	Directional cosine matrix	Translation matrix
o_0-$x_0y_0z_0$					
o_{v1}-$x_{v1}y_{v1}z_{v1}$	$\Delta\theta_{xv0}$, $\Delta\theta_{yv0}$	<5″	$\boldsymbol{T}_{v1}^{\ 0}$=Rot($x_0$,$\Delta\theta_{xv0}$)Rot($y_0$,$\Delta\theta_{yv0}$)	$\boldsymbol{A}_{v1}$	
o_{v2}-$x_{v2}y_{v2}z_{v2}$	ω_v, f_v	0.2 ~30π rad/s, 0.1~15 Hz	$\boldsymbol{T}_{v2}^{\ v1}$=Rot($x_{v1}$,$-\omega_v t$)	$\boldsymbol{A}_{v2}$	
o_{v3}-$x_{v3}y_{v3}z_{v3}$	A_0	0.03 m	$\boldsymbol{T}_{v3}^{\ v2}$=Trans(0, A_0 ,0)Rot(x_{v2} ,$\omega_v t$)	$\boldsymbol{A}_{v3}$	$\boldsymbol{D}_{v3}$
o_{v4}-$x_{v4}y_{v4}z_{v4}$	$\Delta a_x(t)$, $\Delta a_y(t)$, $\Delta a_z(t)$, $\Delta y_x(t)$, $\Delta y_y(t)$, $\Delta y_z(t)$	$\Delta a_x(t)$, $\Delta a_y(t)$, $\Delta a_z(t)$ < 5″, $\Delta y_x(t)$, $\Delta y_y(t)$, $\Delta y_z(t)$ < 5 μm	$\boldsymbol{T}_{v4}^{v3}$ = Trans($\Delta x(t)$,$\Delta y(t)$,$\Delta z(t)$) □Rot(x_{v3} ,$\Delta a_x(t)$)Rot(y_{v3} ,$\Delta a_y(t)$)Rot(z_{v3} ,$\Delta a_z(t)$)	$\boldsymbol{A}_{v4}$	$\boldsymbol{D}_{v4}$
o_{v5}-$x_{v5}y_{v5}z_{v5}$			$\boldsymbol{T}_{v5}^{v4}$=Trans(0, $-A_0\cos\omega_v t$,0)	$\boldsymbol{I}_{3x3}$	$\boldsymbol{D}_{v5}$
o_{v6}-$x_{v6}y_{v6}z_{v6}$	H	1 m	$\boldsymbol{T}_{v6}^{v5}$=Trans(0,0,H)	$\boldsymbol{I}_{3x3}$	$\boldsymbol{D}_{v6}$
o_{v7}-$x_{v7}y_{v7}z_{v7}$	$\Delta\theta_{xv1}$, $\Delta\theta_{yv1}$, $\Delta\theta_{zv1}$, θ_{vi}	<5″	$\boldsymbol{T}_{v7}^{v6}$=Trans(0,0,l_v)Rot(x_{v6} ,$\Delta\theta_{xv1}$) □Rot(y_{v6} ,$\Delta\theta_{yv1}$)Rot(z_{v6},$\Delta\theta_{zv1}$)Rot(x_{v6} ,θ_{vi})	$\boldsymbol{A}_{v7}$	$\boldsymbol{D}_{v7}$
o_p-$x_py_pz_p$	$\Delta\theta_{xv2}$, $\Delta\theta_{yv2}$, $\Delta\theta_{zv2}$	<5″	$\boldsymbol{T}_{p}^{v7}$=Rot(x_{v7} ,$\Delta\theta_{xv2}$)Rot(y_{v7} ,$\Delta\theta_{yv2}$)Rot(z_{v7},$\Delta\theta_{zv2}$)	$\boldsymbol{A}_{v8}$	

(1) Basic coordinate system o_0-$x_0y_0z_0$. Its origin o_0 is located at the center of the center bearing, as shown in Fig.2.

The direction of the axes o_0x_0, o_0y_0, and o_0z_0 respectively coincide with local east, north, and upward, as shown in Fig.1.

(2) Center bearing coordinate system o_{v1}-$x_{v1}y_{v1}z_{v1}$. Its origin o_{v1} coincides with o_0. The main error sources are 2-D perpendicularity $\Delta\theta_{xv0}$ and $\Delta\theta_{yv0}$ about the o_0x_0 and o_0y_0 axes. Based on the Euler angle representation, its H -matrix (homogeneous transformation matrix) with respect to o_0-$x_0y_0z_0$ can be expressed as

$$\boldsymbol{T}_{v1}^{\ 0}=\mathrm{Rot}(x_0,\Delta\theta_{xv0})\mathrm{Rot}(y_0,\Delta\theta_{yv0})=\begin{bmatrix}\boldsymbol{A}_{v1} & \boldsymbol{0}_{3\times1}\\ \boldsymbol{0}_{1\times3} & 1\end{bmatrix}_{4\times4} \tag{2}$$

where Rot (x_0, $\Delta\theta_{xv0}$) indicates that the coordinate system o_0-$x_0y_0z_0$ rotates about o_0x_0 axis by angle $\Delta\theta_{xv0}$ and matrix $\boldsymbol{A}_{v1}$ is the directional cosine matrix that can be expressed as

$$\boldsymbol{A}_{v1}=\begin{bmatrix}1 & 0 & \Delta\theta_{yv0}\\ 0 & 1 & -\Delta\theta_{xv0}\\ -\Delta\theta_{yv0} & \Delta\theta_{xv0} & 1\end{bmatrix} \tag{3}$$

(3) Rotation coordinate system o_{v2}-$x_{v2}y_{v2}z_{v2}$. Its origin o_{v2} coincides with o_{v1}. The direction of $o_{v2}x_{v2}$ coincides with $o_{v1}x_{v1}$ and the coordinate system o_{v1}-$x_{v1}y_{v1}z_{v1}$ rotates about $o_{v1}x_{v1}$ axis at angular velocity -ω_v rad/s (the vibration frequency is $f_v = \omega_v/2\pi$). The expression of $\boldsymbol{T}_{v2}^{\ v1}$ with respect to o_{v1}-$x_{v1}y_{v1}z_{v1}$ is shown in Table 2, where the directional cosine matrix is $\boldsymbol{A}_{v2}$.

(4) End bearing coordinate system o_{v3}-$x_{v3}y_{v3}z_{v3}$. The coordinate system o_{v2}-$x_{v2}y_{v2}z_{v2}$ is first translated along the $o_{v2}y_{v2}$ axis line with the displacement A_0. Then the origin o_{v3} is located at the center of the end bearing, as shown in

Fig.2. Next, the coordinate system rotates about $o_{v2}x_{v2}$ axis at angular velocity ω_v. The H -matrix $\boldsymbol{T}_{v3}^{v2}$ of o_{v3}-$x_{v3}y_{v3}z_{v3}$ with respect to o_{v2}-$x_{v2}y_{v2}z_{v2}$ is shown in Table 2, where Trans (0, A_0, 0) means that the coordinate system o_{v2}-$x_{v2}y_{v2}z_{v2}$ translates along the $o_{v2}y_{v2}$ axis line with the displacement A_0, while the translation matrix $\boldsymbol{D}_{v3}$ can be expressed as

$$\boldsymbol{D}_{v3}=\begin{bmatrix}0 & A_0 & 0\end{bmatrix}^{\mathrm{T}}. \tag{4}$$

(5) End bearing working coordinate system o_{v4}-$x_{v4}y_{v4}z_{v4}$. Its origin o_{v4} coincides with o_{v3}. Due to the manufacturing tolerance and assembly errors, the main error sources are 2-D perpendicularity a_{vx0} and a_{vy0}, parasitic rotation errors ($\Delta a_x(t)$, $\Delta a_y(t)$, and $\Delta a_z(t)$), and parasitic translation errors ($\Delta x(t)$, $\Delta y(t)$, and $\Delta z(t)$). In addition, the linear vibration table's output waveform deviation can be considered parasitic translation, which also contains high-order harmonic components along the $o_{v3}x_{v3}$ axis line. Then, the H -matrix of o_{v4}-$x_{v4}y_{v4}z_{v4}$ with respect to o_{v3}-$x_{v3}y_{v3}z_{v3}$ is $\boldsymbol{T}_{v4}^{v3}$, where the directional cosine matrix is $\boldsymbol{A}_{v4}$ and the translation matrix is $\boldsymbol{D}_{v4}$.

Taking $\Delta a_x(t)$ and $\Delta z(t)$ as examples, when only the first-order and second-order of the Fourier transforms are taken into account, $\Delta a_x(t)$ and $\Delta z(t)$ can be expressed as

$$\Delta a_x(t)=a_{vx0}+\sum_{j=1}^{2}\left(a_{xsj}\sin j\omega_v t+a_{xcj}\cos j\omega_v t\right), \tag{5}$$

$$\Delta z(t)=\sum_{j=1}^{2}\left(Z_{sj}\sin j\omega_v t+Z_{cj}\cos j\omega_v t\right). \tag{6}$$

(6) Vertical vibration coordinate system o_{v5}-$x_{v5}y_{v5}z_{v5}$. It is formed by translating the coordinate system o_{v4}-$x_{v4}y_{v4}z_{v4}$ along the $o_{v4}y_{v4}$ axis with the displacement $-A_0\cos\omega_v t$, as shown in Fig.2. Its H -matrix $\boldsymbol{T}_{v5}^{v4}$ with respect to o_{v4}-$x_{v4}y_{v4}z_{v4}$ is shown in Table 2, where the directional cosine matrix is $\boldsymbol{I}_{3\times3}$ (means identity matrix) and the translation matrix is $\boldsymbol{D}_{v5}$.

(7) Table top coordinate system o_{v6}-$x_{v6}y_{v6}z_{v6}$. It is formed by translating the coordinate system o_{v5}-$x_{v5}y_{v5}z_{v5}$ along the $o_{v5}z_{v5}$ axis line with displacement H. Its H -matrix $\boldsymbol{T}_{v6}^{v5}$ with respect to o_{v5}-$x_{v5}y_{v5}z_{v5}$ is shown in Table 2, where the directional cosine matrix is $\boldsymbol{I}_{3\times3}$ and the translation matrix is $\boldsymbol{D}_{v6}$.

(8) Indexing head coordinate system o_{v7}-$x_{v7}y_{v7}z_{v7}$. It is formed by translating the coordinate system o_{v6}-$x_{v6}y_{v6}z_{v6}$ along the $o_{v6}z_{v6}$ axis line with displacement l_v. The main error sources are installation angle errors ($\Delta\theta_{xv1}$, $\Delta\theta_{yv1}$, and $\Delta\theta_{zv1}$) about three axes. When the rotation angle about the $o_{v7}x_{v7}$ axis of indexing head is θ_{vi} (i = 0,1,…, n−1), its H -matrix $\boldsymbol{T}_{v7}^{v6}$ of o_{v7}-$x_{v7}y_{v7}z_{v7}$ with respect to o_{v6}-$x_{v6}y_{v6}z_{v6}$ is shown in Table 2, where the directional cosine matrix is $\boldsymbol{A}_{v7}$ and the translation matrix is $\boldsymbol{D}_{v7}$.

(9) PIGA coordinate system o_p-$x_py_pz_p$. Without considering the installation displacement errors of PIGA, the origin o_p is the effective mass center (EMC) of PIGA that coincides with o_{v7}. The input axis, pendulous axis, and output axis of PIGA coincide with o_px_p, o_py_p, and o_pz_p, respectively. The main error sources are installation angle errors about the three axes of o_{v7}-$x_{v7}y_{v7}z_{v7}$ ($\Delta\theta_{xv2}$, $\Delta\theta_{yv2}$, and $\Delta\theta_{zv2}$). The H -matrix $\boldsymbol{T}_p^{v7}$ of o_p-$x_py_pz_p$ with respect to o_{v7}-$x_{v7}y_{v7}z_{v7}$ is shown in Table 2, where the directional cosine matrix is $\boldsymbol{A}_{v8}$.

According to the characteristics of the linear vibration table and established coordinate systems, the main parameters are summarized as shown in Table 2. It is shown that the main error sources are parasitic errors caused by the vibration working mechanisms and attitude (position) errors caused by the installation (positioning) devices.

3. Inputs of PIGA on precision linear vibration table

The input accelerations of PIGA consist of the sinusoidal accelerations generated by the linear vibration, Coriolis accelerations, and gravitational accelerations. The complete input accelerations of PIGA along the three axes are obtained:

$$\begin{bmatrix}a_O\\a_P\\a_I\end{bmatrix}=\begin{bmatrix}a_{vx}\\a_{vy}\\a_{vz}\end{bmatrix}+\begin{bmatrix}a_{cx}\\a_{cy}\\a_{cz}\end{bmatrix}+\begin{bmatrix}a_{gx}\\a_{gy}\\a_{gz}\end{bmatrix} \tag{7}$$

According to the coordinate systems, the H -matrix of o_{v6}-$x_{v6}y_{v6}z_{v6}$ with respect to o_0-$x_0y_0z_0$ can be expressed as

$$\boldsymbol{T}_{v2}^{v1}\boldsymbol{T}_{v3}^{v2}\boldsymbol{T}_{v4}^{v3}\boldsymbol{T}_{v5}^{v4}\boldsymbol{T}_{v6}^{v5}=\begin{bmatrix}\boldsymbol{A}_{v2}\boldsymbol{A}_{v3}\boldsymbol{A}_{v4} & \boldsymbol{D}_v\\ \boldsymbol{0} & 1\end{bmatrix} \tag{8}$$

where $\boldsymbol{D}_v=\boldsymbol{A}_{v2}\boldsymbol{A}_{v3}\boldsymbol{A}_{v4}\left(\boldsymbol{D}_{v6}+\boldsymbol{D}_{v5}\right)+\boldsymbol{A}_{v2}\boldsymbol{A}_{v3}\boldsymbol{D}_{v4}+\boldsymbol{A}_{v2}\boldsymbol{D}_{v3}$.

Thus, the sinusoidal input accelerations (a_{vx}, a_{vy}, and a_{vz}) generated by the linear vibration table along the OA, PA, and IA axes of PIGA are:

$$\begin{bmatrix} a_{vx} & a_{vy} & a_{vz} \end{bmatrix}^{T} = \left(\boldsymbol{A}_{v2} \boldsymbol{A}_{v3} \boldsymbol{A}_{v4} \boldsymbol{A}_{v7} \boldsymbol{A}_{p} \right)^{T} \frac{\mathrm{d}^2 \boldsymbol{D}_{v}}{\mathrm{d}t^2} \tag{9}$$

Coriolis acceleration components (a_{cx}, a_{cy}, and a_{cz}) along the three axes of PIGA are calculated as follows:

$$\begin{aligned} &\begin{bmatrix} a_{cx} & a_{cy} & a_{cz} \end{bmatrix}^{T} \\ &= 2\begin{bmatrix} 0 & \omega_{ie}\cos\lambda & \omega_{ie}\sin\lambda \end{bmatrix}^{T} \times \begin{bmatrix} 0 & 0 & -A_0\omega_v\cos\omega_v t \end{bmatrix}^{T} \\ &= \begin{bmatrix} -2A_0\omega_{ie}\omega_v\cos\lambda\cos\omega_v t & 0 & 0 \end{bmatrix}^{T} \end{aligned} \tag{10}$$

where ω_{ie} is the turn rate of the Earth and λ is the local latitude.[23]

Gravitational acceleration components (a_{gx}, a_{gy}, and a_{gz}) along the three axes of PIGA are calculated:

$$\begin{bmatrix} a_{gx} & a_{gy} & a_{gz} \end{bmatrix}^{T} = \left(\boldsymbol{A}_{v1} \boldsymbol{A}_{v2} \boldsymbol{A}_{v3} \boldsymbol{A}_{v4} \boldsymbol{A}_{v7} \boldsymbol{A}_{p} \right)^{T} \begin{bmatrix} 0 & 0 & g \end{bmatrix}^{T} \tag{11}$$

where g is the local acceleration reacted to gravity and can be calculated by the typical equation.[24]

Then, without considering the high-order harmonic acceleration components generated by the parasitic error sources, the complete expression of a_I can be deduced by substituting Eqs.(5) and (6) into Eq.(7):

$$\begin{aligned} a_I =& g\cos\theta_{vi} - \left(\Delta\theta_{xv0} + \Delta\theta_{vx} + a_{vx0}\right) g\sin\theta_{vi} + \frac{1}{2} a_{xs1} A_0 \omega_v^2 \sin\theta_{vi} - a_{xs1} g\sin\theta_{vi}\sin\omega_v t - a_{xc1} g\sin\theta_{vi}\cos\omega_v t - a_{xs2} g\sin\theta_{vi}\sin 2\omega_v t - a_{xc2} g\sin\theta_{vi}\cos 2\omega_v t \\ &+ \left(\left(a_{x0} A_0 + \frac{1}{2} a_{xc2} A_0 - Z_{c1} \right)\cos\theta_{vi} + \left(Y_{c1} - a_{xc1} H + \frac{1}{2} a_{xs2} A_0 \right)\sin\theta_{vi} \right)\omega_v^2 \cos\omega_v t \\ &+ \left(\left(A_0 + \frac{1}{2} a_{xs2} A_0 - Z_{s1} \right)\cos\theta_{vi} + \left(Y_{s1} - a_{xs1} H - \left(\Delta\theta_{vi} + \Delta\theta_{vx} + a_{x0} - \frac{1}{2} a_{xc2} \right) A_0 \right)\sin\theta_{vi} \right)\omega_v^2 \sin\omega_v t \\ &+ \left(\left(2a_{xs1} - 4Z_{s2} \right)\cos\theta_{vi} + \left(4Y_{s2} - 4a_{xs2} H - \frac{1}{2} a_{xc1} \right)\sin\theta_{vi} \right) A_0 \omega_v^2 \sin 2\omega_v t + \left(\left(2a_{xc1} - 4Z_{c2} \right)\cos\theta_{vi} + \left(4\left(Y_{c2} - a_{xc2} H \right) + \frac{1}{2} a_{xs1} \right)\sin\theta_{vi} \right) A_0 \omega_v^2 \cos 2\omega_v t \\ &+ \left(\frac{9}{2} a_{xs2}\cos\theta_{vi} - \frac{1}{2} a_{xc2}\sin\theta_{vi} \right) A_0 \omega_v^2 \sin 3\omega_v t + \left(\frac{9}{2} a_{xc2}\cos\theta_{vi} + \frac{1}{2} a_{xs2}\sin\theta_{vi} \right) A_0 \omega_v^2 \cos 3\omega_v t \end{aligned} \tag{12}$$

where $\Delta\theta_{vy} = \Delta\theta_{yv1} + \Delta\theta_{yv2}$ and $\Delta\theta_{vx} = \Delta\theta_{xv0} + \Delta\theta_{xv1} + \Delta\theta_{xv2}$.

Ideally, the nominal input acceleration a_{IA} of PIGA along the IA axis can be expressed as

$$a_{IA} = \left(A_0 \omega_v^2 \sin\omega_v t + 1g \right)\cos\theta_{vi} \tag{13}$$

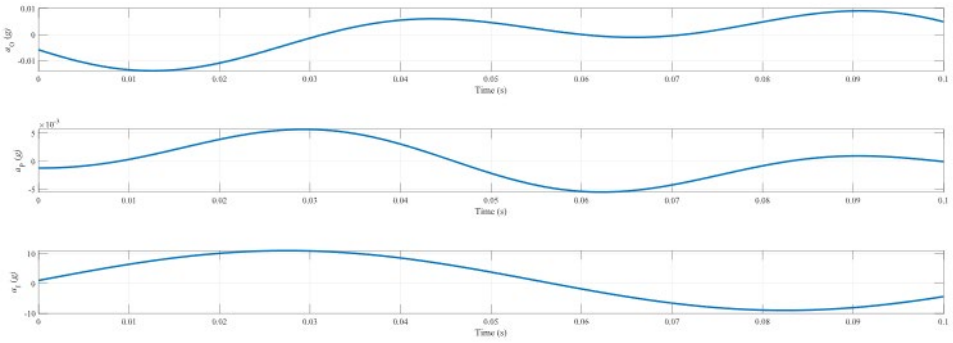

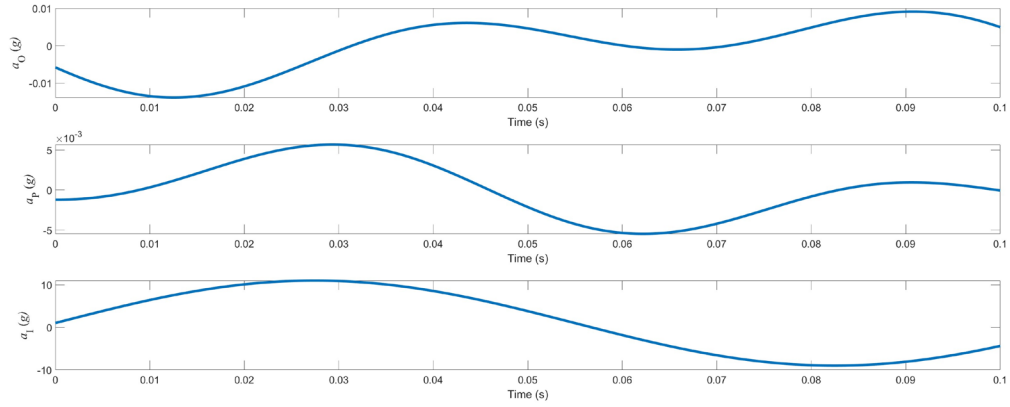

(a) Simulation results of input accelerations of PIGA

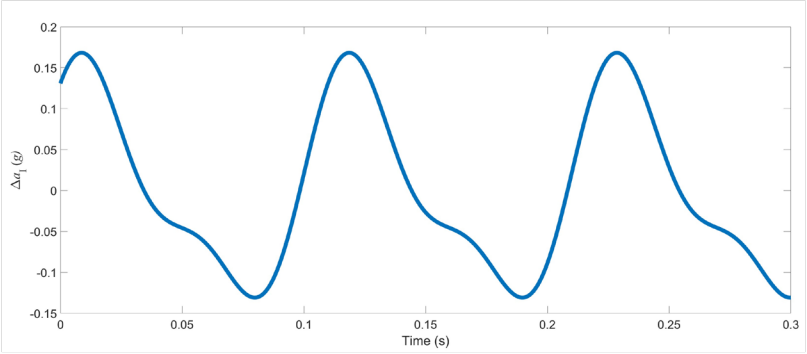

(b) Simulation results of Δa_I

Fig. 3 Simulation results of input accelerations and acceleration errors.

When $\theta_{vi} = 0$, the simulations are constructed to describe the input accelerations along the three axes of PIGA as shown in Fig.3(a). The peak-to-peak values of a_O and a_P are equal to 0.0230 g and 0.0112 g, respectively, due to the error sources in Eqs.(12) and (13). The simulation results are shown in Fig.3(b) for the acceleration error along the IA axis equal to $\Delta a_I = a_{IA} - a_I$. It can be observed that errors in Eq.(12) cause significant distortion of the vibration wave form, while the amplitude of acceleration errors are higher than 0.15 g. The uncertainty of a_{IA} can be calculated by

$$\sigma a_{\mathrm{IA}} = \sqrt{\left(\frac{\partial a_{\mathrm{IA}}}{\partial \omega_{\mathrm{v}}}\sigma_{\omega_{\mathrm{v}}}\right)^2 + \left(\frac{\partial a_{\mathrm{IA}}}{\partial A_0}\sigma_{A_0}\right)^2 + \left(\frac{\partial a_{\mathrm{IA}}}{\partial \theta_{vi}}\sigma_{\theta_{vi}}\right)^2 + \left(\frac{\partial a_{\mathrm{IA}}}{\partial g}\sigma_g\right)^2}, \tag{14}$$

where σ_{ω_v}, σ_{A_0}, $\sigma_{\theta_{vi}}$, and σ_g are the uncertainties of ω_{v}, A_0, θ_{vi}, and g, respectively.

Based on the aforementioned simulations, the initial values of σ_{ω_v}, σ_{A_0}, and $\sigma_{\theta_{vi}}$ are set as 1.0×10^{-10} Hz, 1.0×10^{-10}m, and 1.0×10^{-10} rad, respectively. Then, the values of σa_{IA} range from 1.0×10^{-4} m·s^{-2} to 3.4×10^{-7} m·s^{-2}, when the maximum values of σ_g range from 1.0×10^{-5} m·s^{-2} to 1.0×10^{-7} m·s^{-2}. It is noted that the calculated uncertainty of g should be less than 1.0×10^{-7} m·s^{-2} to ensure the accuracy of input accelerations. In addition, when $\sigma_g = 1.0\times10^{-7}$ m·s^{-2} and $\sigma_g = 1.0\times10^{-8}$ m·s^{-2}, the maximum values of σa_{IA} are 3.4×10^{-7} m·s^{-2} and 3.2×10^{-7} m·s^{-2}, which only have a small difference. Thus, the gravitational acceleration g needs to be accurate at the eighth significant digit in this paper, that is, 1 g = 9.8016093 m·s^{-2}, when the local latitude λ is 39.94° and the altitude is 2.7 m.

The input angular velocities along the three PIGA axes consist of the angular velocity component of the earth rotation and the parasitic rotation errors:

$$\left[\omega_{\mathrm{O}} \quad \omega_{\mathrm{P}} \quad \omega_{\mathrm{I}}\right]^{\mathrm{T}} = \left(\boldsymbol{A}_{\mathrm{v1}}\boldsymbol{A}_{\mathrm{v2}}\boldsymbol{A}_{\mathrm{v3}}\boldsymbol{A}_{\mathrm{v4}}\boldsymbol{A}_{\mathrm{v7}}\boldsymbol{A}_{\mathrm{p}}\right)^{\mathrm{T}}\left[0 \quad \omega_{\mathrm{ie}}\cos\lambda \quad \omega_{\mathrm{ie}}\sin\lambda\right]^{\mathrm{T}} + \left(\boldsymbol{A}_{\mathrm{v7}}\boldsymbol{A}_{\mathrm{p}}\right)^{\mathrm{T}}\left[\frac{\mathrm{d}\Delta a_{\mathrm{x}}(t)}{\mathrm{d}t} \quad \frac{\mathrm{d}\Delta a_{\mathrm{y}}(t)}{\mathrm{d}t} \quad \frac{\mathrm{d}\Delta a_{\mathrm{z}}(t)}{\mathrm{d}t}\right]^{\mathrm{T}} \tag{15}$$

4. Error calibration model of PIGA

Actually, numerous factors can affect the measurement accuracy of PIGA, such as the design and assembly errors, disparities in elasticity, mass imbalances, elastic torque, static friction torque, and vibration interference torque. Thus, the error model of PIGA testing in the high-g environment should be deduced firstly:

$$\dot{\alpha}=k_0+k_z a_{\mathrm{I}}+k_{zz}a_{\mathrm{I}}^{\ 2}+k_3 a_{\mathrm{I}}^{\ 3}+k_x a_{\mathrm{O}}^{\ 2}+k_y a_{\mathrm{P}}^{\ 2}+k_{oq}a_{\mathrm{I}}\left|a_{\mathrm{I}}\right|-\omega_{\mathrm{I}}+\varepsilon \tag{16}$$

where k_0 is the bias (rad·s^{-1}), k_z is the scale factor [(rad·s^{-1})/g] and $k_z = ml/H$, k_{zz} is the second-order error coefficient [(rad·s^{-1})/g^2], k_3 is the third-order error coefficient [(rad·s^{-1})/g^3], k_x and k_y are the second-order error coefficient along the OA axis line and PA axis line [(rad·s^{-1})/g] respectively, k_{oq} is an odd quadratic error coefficient [(rad·s^{-1})/g^2], and ε is the random error.

According to the simulation results of a_{O}, the maximum value of the error term $k_x a_{\mathrm{O}}^2$ is less than 10^{-8} rad/s when the vibration frequency is 20 Hz; hence, $k_x a_{\mathrm{O}}^2$ can be assumed as negligible. This is another advantage of the linear vibration table test, i.e., it can automatically eliminate the influence of Coriolis acceleration if the direction of the OA axis refers to the east. The output of PIGA is the average precession angular velocity obtained by counting the number of output pulses P_{A} (the number of output pulses of PIGA is 16384 per period). When the position of indexing head is $\theta_{\mathrm{v}i}$ (i = 0, 1, 2, …) and the angular velocity of the crank disk is $\omega_{\mathrm{v}j}$ (j = 0,1,2, …), the average precession angular velocity of PIGA during the test time T_{m} (i,j) can be calculated as follows:

$$\begin{aligned}\bar{\dot{\alpha}}(i,j)&=\frac{2\pi P_{\mathrm{A}}}{16384T_{\mathrm{m}}(i,j)}=\frac{1}{T_{\mathrm{m}}(i,j)}\int_0^{T_{\mathrm{m}}(i,j)}\dot{\alpha}\mathrm{d}t\\&=k_0+k_z\cos\theta_{vi}-k_z\Delta\theta_{vi}\sin\theta_{vi}-\omega_{\mathrm{ie}}\sin\lambda\cos\theta_{vi}+\omega_{\mathrm{ie}}\cos\lambda\sin\theta_{vi}-k_z\left(\Delta\theta_{\mathrm{xv0}}+\Delta\theta_{\mathrm{vx}}+a_{\mathrm{vx0}}\right)\sin\theta_{vi}\\&+\frac{1}{2}a_{\mathrm{xs1}}\left(k_z-k_{zz}\cos\theta_{vi}\right)A_0{\omega_{vj}}^2/g\sin\theta_{vi}+k_{oq}\cos\theta_{vi}\left|\cos\theta_{vi}\right|+k_{zz}\cos^2\theta_{vi}+\frac{1}{2}\left(1+a_{\mathrm{xs2}}-\frac{2Z_{\mathrm{s1}}}{A_0}\right)k_{zz}{A_0}^2{\omega_{vj}}^4/g^2\cos^2\theta_{vi}\\&+\frac{1}{2}\left(1+a_{\mathrm{xs2}}-\frac{2Z_{\mathrm{s1}}}{A_0}\right)k_y{A_0}^2{\omega_{vj}}^4/g^2\sin^2\theta_{vi}+k_y\sin^2\theta_{vi}+k_3\cos^3\theta_{vi}+\frac{3}{2}k_3{A_0}^2{\omega_{vj}}^4/g^2\cos^3\theta_{vi}+\frac{1}{2}\left(k_{zz}-k_y\right)\Delta\varphi{A_0}^2{\omega_{vj}}^4/g^2\cos\theta_{vi}\sin\theta_{vi}+\varepsilon\end{aligned} \tag{17}$$

where $\Delta\varphi=2\left(Y_{\mathrm{s1}}-a_{\mathrm{xs1}}H\right)/A_0+2\Delta\theta_{\mathrm{vx}}+2a_{\mathrm{vx0}}-a_{\mathrm{xc2}}$.

In Eq.(17), the main error sources of the average precession angular velocity include the harmonic terms of the parasitic rotation, the first order sinusoidal term of the output waveform deviation Z_{s1}, and position errors $\Delta\varphi$. When the value of $\Delta\varphi$ is greater than 0.001 rad, the new error term $(k_{zz}-k_y)\,\Delta\varphi$ is excited and significantly affects the calibration uncertainty of PIGA. Thus, the installation angle errors should be less than 1×10^{-3} rad to modify the error calibration model of PIGA. In addition, the main error sources of the output of PIGA are the counting and timing errors defined in Eq.(17). Thus, the calibration method of PIGA testing within integer-periods is proposed to suppress the influence of the counting error.

When $\theta_{\mathrm{v}i}$ = 0, the nominal input acceleration of PIGA along the IA axis is: $a_{\mathrm{N}}=A\sin\omega_{\mathrm{v}}t+g$, where $A=A_0{\omega_{\mathrm{v}}}^2$. The input acceleration and output pulse of PIGA within integer-periods are shown in Fig.4, where the number of vibration period is N_p, the vibration time is $T_{\mathrm{N}}=2\pi N_{\mathrm{p}}/\omega_{\mathrm{v}}$, t_1 is the period of the first time that the read head has moved to the zero position, and $t_2=t_1+2\pi N_{\mathrm{p}}/\omega_{\mathrm{v}}-T_{\mathrm{m}}$. Although electromagnetic interference from the test equipment and environment could be efficiently decreased by integrating the input accelerations within the integer precession periods of PIGA, the error interference generated during 0~t_1 and T_{m}~T_{N} should also affect the measurement accuracy of PIGA. Thus, the corresponding errors should be considered and compensated in PIGA output.

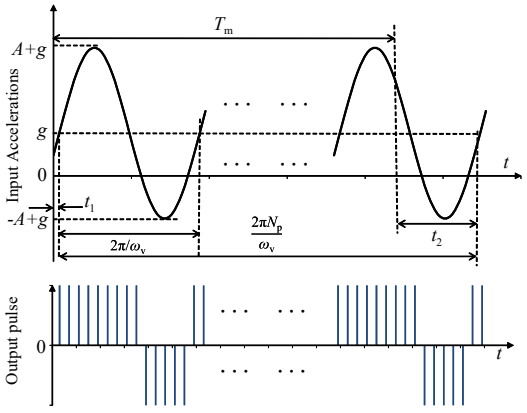

Fig. 4 Input accelerations and output pulses of PIGA testing within integer-periods precession.

The average precession angular velocity of PIGA is:

$$\bar{\dot{\alpha}}(0,j)=\frac{1}{T_{\mathrm{m}(0,j)}}\left(\int_0^{t_{1(0,j)}}\dot{\alpha}(0,j)\mathrm{d}t+\int_{t_1}^{t_1+\frac{2\pi N_{\mathrm{p}(0,j)}}{\omega_{\mathrm{v}j}}}\dot{\alpha}(0,j)\mathrm{d}t-\int_{T_{\mathrm{m}(0,j)}}^{T_{\mathrm{m}(0,j)}+t_{2(0,j)}}\dot{\alpha}(0,j)\mathrm{d}t\right) \tag{18}$$

According to Eq. (18), the static errors can be eliminated by subtracting the PIGA output in the static state. The calibration equation is obtained as

$$\frac{1}{T_{\mathrm{m}(i,j)}}\int_0^{T_{\mathrm{m}(i,j)}}\dot{\alpha}(i,j)\mathrm{d}t-\frac{1}{T_{\mathrm{m}(i,j)}}\int_0^{T_{\mathrm{m}(i,j)}}\dot{\alpha}(i,0)\mathrm{d}t=L_1(i,j)k_z+L_2(i,j)k_{zz}+L_3(i,j)k_y+L_4(i,j)k_3 \tag{19}$$

where

$$L_1(i,j)=\left(\frac{1}{2}a_{\mathrm{xs1}}\sin\theta_{\mathrm{v}i}+\frac{1}{\omega_{\mathrm{v}j}T_{\mathrm{m}(i,j)}}(\cos\omega_{\mathrm{v}j}t_{2(i,j)}-\cos\omega_{\mathrm{v}j}t_{1(i,j)})\right)A_j/g$$

$$L_2(i,j)=\frac{1}{2}\left(1-\frac{2Z_{\mathrm{s1}}}{A_0}\right)A_j^{\,2}/g^2\cos^2\theta_{\mathrm{v}i}+\frac{2A_j\cos\theta_{\mathrm{v}i}}{\omega_{\mathrm{v}j}T_{\mathrm{m}(i,j)}}(\cos\omega_{\mathrm{v}j}t_{1(i,j)}-\cos\omega_{\mathrm{v}j}t_{2(i,j)})+\frac{A_j^{\,2}/g^2\cos^2\theta_{\mathrm{v}i}}{4\omega_{\mathrm{v}j}T_{\mathrm{m}(i,j)}}(-\sin2\omega_{\mathrm{v}j}t_{1(i,j)}+\sin2\omega_{\mathrm{v}j}t_{2(i,j)})$$

$$L_3(i,j)=\frac{1}{2}\left(1-\frac{2Z_{\mathrm{s1}}}{A_0}\right)A_j^{\,2}/g^2\sin^2\theta_{\mathrm{v}i}+\frac{2A_j\sin\theta_{\mathrm{v}i}}{\omega_{\mathrm{v}j}T_{\mathrm{m}(i,j)}}(\cos\omega_{\mathrm{v}j}t_{1(i,j)}-\cos\omega_{\mathrm{v}j}t_{2(i,j)})+\frac{A_j^{\,2}/g^2\sin^2\theta_{\mathrm{v}i}}{4\omega_{\mathrm{v}j}T_{\mathrm{m}(i,j)}}(-\sin2\omega_{\mathrm{v}j}t_{1(i,j)}+\sin2\omega_{\mathrm{v}j}t_{2(i,j)})$$

$$L_4(i,j)=\frac{3}{2}A_j^{\,2}/g\cos^2\theta_i+\frac{3A_j^{\,2}/g\cos^2\theta_{\mathrm{v}i}}{4\omega_{\mathrm{v}j}T_{\mathrm{m}(i,j)}}(\sin2\omega_{\mathrm{v}j}t_{2(i,j)}-\sin2\omega_{\mathrm{v}j}t_{1(i,j)})+\frac{(12gA_j\cos\theta_{\mathrm{v}i}+3A_j^{\,3}/g^3\cos^3\theta_{\mathrm{v}i})}{4\omega_{\mathrm{v}j}T_{\mathrm{m}(i,j)}}(\cos\omega_{\mathrm{v}j}t_{1(i,j)}-\cos\omega_{\mathrm{v}j}t_{2(i,j)})$$
$$+\frac{A_j^{\,3}/g^3\cos^3\theta_{\mathrm{v}i}}{12\omega_{\mathrm{v}j}T_{\mathrm{m}(i,j)}}(\cos3\omega_{\mathrm{v}j}t_{2(i,j)}-\cos3\omega_{\mathrm{v}j}t_{1(i,j)})$$

Compared with Eq.(17), it is shown that the calibration model of PIGA precession within the integer periods can be used to calibrate the nonlinear error terms of PIGA more accurately after compensating for the extra outputs generated by linear vibrating without integer periods.

5. Calibration process design

The complete test process for PIGA offline calibration on the linear vibration table is proposed as shown in Fig.5. The test process is divided into three parts:

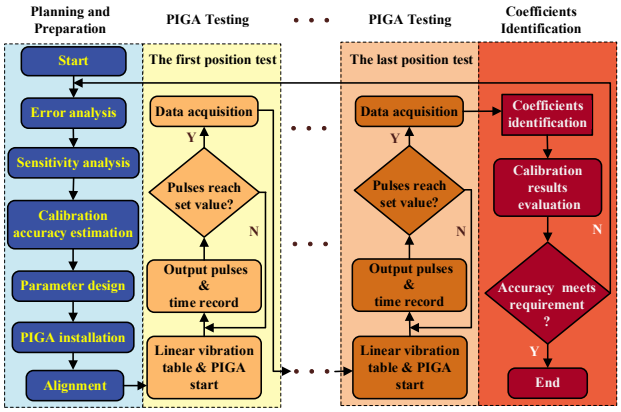

Fig. 5 Test flowchart of PIGA within integer-period precession on linear vibration table.

5.1. Planning and Preparation

Error and sensitivity analyses should be conducted before PIGA test to analyze the influences of the main error sources and test positions. Then, calibration uncertainty can be estimated to pre-evaluate the calibration results. According to the analyses and calculation results mentioned above, the corresponding parameters of the calibration test should be reasonably designed. The detailed process is presented below.

5.1.1. Error analysis

The error analysis of the input acceleration of PIGA was provided in Section 3. In order to illustrate the influence of error sources on the accuracy requirements of the linear vibration table, the numerical calculations are shown in Table 3.

It is shown that the error accelerations caused by installation errors, parasitic rotation errors, and parasitic translation errors strongly affect the input accelerations of PIGA. When the nominal input acceleration a_{IA} equals 10 g, the acceleration errors caused by installation angle and parasitic rotation errors are approximately 2.5×10^{-4} g. Moreover, the acceleration errors caused by the parasitic translation errors and output waveform deviation are approximately equal to 1.7×10^{-3} g.

Table 3 Analysis of error accelerations on linear vibration table

Error source	Value	Error acceleration (g)
$\Delta\theta_{xv0}$, $\Delta\theta_{yv0}$	5″	2.5×10^{-5}
$\Delta\alpha_x(t)$, $\Delta\alpha_y(t)$	2″	1×10^{-4}
$\Delta\alpha_z(t)$	5″	2.5×10^{-4}
$\Delta x(t)$, $\Delta y(t)$, $\Delta z(t)$	5 μm	1.67×10^{-3}
$\Delta\theta_{xv1}$, $\Delta\theta_{yv1}$, $\Delta\theta_{zv1}$	5″	2.5×10^{-4}

5.1.2. Sensitivity analysis

According to the error calibration model in Section 4, the Least-Squares (LS) method is adopted to identify the nonlinear error coefficients as follows:

$$\hat{\boldsymbol{K}}=\left(\boldsymbol{L}^{\mathrm{T}}\boldsymbol{L}\right)^{-1}\boldsymbol{L}^{\mathrm{T}}\boldsymbol{Y} \tag{20}$$

where

$$\hat{\boldsymbol{K}}=\begin{bmatrix}\hat{k}_z & \hat{k}_{zz} & \hat{k}_y & \hat{k}_3\end{bmatrix}^{\mathrm{T}}$$

$$\boldsymbol{L}=\begin{bmatrix}L_1(0,j) & L_2(0,j) & L_3(0,j) & L_4(0,j)\\ \vdots & \vdots & \vdots & \vdots\\ L_1(n,j) & L_2(n,j) & L_3(n,j) & L_4(n,j)\end{bmatrix}$$

$$\boldsymbol{Y}=\begin{bmatrix}\bar{\alpha}(0,j)-\bar{\alpha}(0,0)\\ \mathrm{M}\\ \bar{\alpha}(n,j)-\bar{\alpha}(n,0)\end{bmatrix}$$

The residual matrix $\boldsymbol{e}$ and the standard deviation of the residual σ can be calculated as follows:

$$\begin{cases}\boldsymbol{e}=\boldsymbol{Y}-\boldsymbol{L}\hat{\boldsymbol{K}}\\ \sigma=\sqrt{\boldsymbol{e}^{\mathrm{T}}\boldsymbol{e}/(n-4)}\end{cases} \tag{21}$$

It is assumed that the output uncertainty of PIGA is constant. When the information matrix is $\boldsymbol{Q}=\boldsymbol{L}^{\mathrm{T}}\boldsymbol{L}$, the standard deviation of the nonlinear error coefficients can be obtained as

$$\begin{aligned}&\left[\sigma\left(\hat{k}_z\right)\quad\sigma\left(\hat{k}_{zz}\right)\quad\sigma\left(\hat{k}_y\right)\quad\sigma\left(\hat{k}_3\right)\right]^{\mathrm{T}}\\ &=\left[\sqrt{d_{11}}\quad\sqrt{d_{22}}\quad\sqrt{d_{33}}\quad\sqrt{d_{44}}\right]^{\mathrm{T}}\sigma\end{aligned} \tag{22}$$

where d_{11}, d_{22}, d_{33}, and d_{44} are main diagonal elements of $\boldsymbol{Q}^{-1}$.

The calibration uncertainty of the nonlinear error coefficients can be expressed as the standard deviation of the nonlinear error coefficients in Eq.(21). Thus, the calibration uncertainty should be improved by increasing the number of the test position n and decreasing the value of the main diagonal elements of $\boldsymbol{Q}^{-1}$. Although increasing test positions can effectively decrease the calibration uncertainty, the test cost and efficiency should also be increased. Therefore, it is necessary to scientifically and reasonably optimize the test positions to meet the calibration uncertainty and ensure the test efficiency.

Currently, the most common inertial calibration test method is optimizing the matrix $\boldsymbol{Q}$ based on the D-optimal criterion. In order to accurately identify the coefficients in the PIGA error calibration model via the LS method, the rank of $\boldsymbol{Q}$ must be greater than the number of coefficients, and the value of the determinant det ($\boldsymbol{Q}$) should be designed as high as possible.

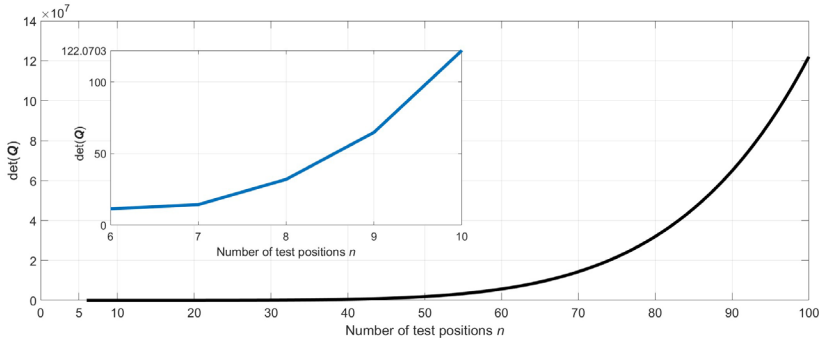

Fig. 6. Relationship between det($\boldsymbol{Q}$) and the number of test positions

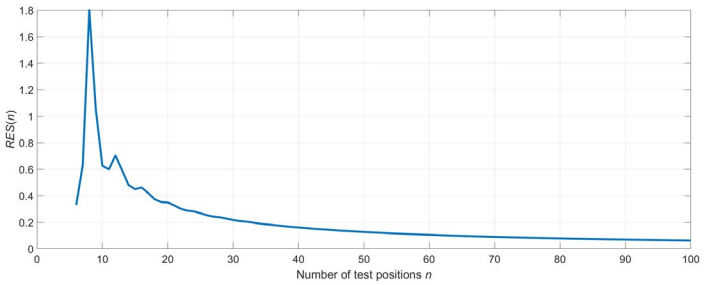

Fig. 7 Relationship between RES and the number of test positions.

The values of det ($\boldsymbol{Q}$) for different numbers of test positions are shown in Fig.6 for the test angle positions of PIGA taken as interval angles on the indexing head. An exponential growth trend of det ($\boldsymbol{Q}$) can be observed with an increase in n.

In order to evaluate the sensitivity of det ($\boldsymbol{Q}$) and optimize the test positions, the relative sensitivity function is constructed as

$$\mathrm{RES}(n)=\frac{\det\left(\boldsymbol{Q}(n)\right)-\det\left(\boldsymbol{Q}(n-1)\right)}{\det\left(\boldsymbol{Q}(n)\right)\cdot\Delta N} \tag{23}$$

where $\Delta N=n-(n-1)=1$.

The calculation results of RES(n) in Fig.7 indicate that the value of relative sensitivity sharply increases when n is less than nine, and the maximum value is approximately equal to 1.8 for n = 9. It is illustrated that the 9-position test is the most sensitive and effective. Moreover, the value of RES(n) declines when $n \geq 10$ and the curve gradually flattens when $n \geq 40$. Consequently, an excess of test positions may be unsuitable for high-efficiency tests, whereas the optimal range of n is usually from 9 to 40.

5.1.3. Calibration uncertainty estimation

As the expression of the average precession angular velocity of PIGA has been given in Eq.(17), the propagation of the measurement uncertainty of $\bar{\dot{\alpha}}(i,j)$ can be expressed as follows:

$$\sigma_{\bar{\dot{\alpha}}}(i,j)=\sqrt{\left(\frac{\partial\bar{\dot{\alpha}}(i,j)}{\partial P_{i,j}}\sigma_{\mathrm{P}}\right)^2+\left(\frac{\partial\bar{\dot{\alpha}}(i,j)}{\partial T_{\mathrm{m}(i,j)}}\sigma_{\mathrm{T}}\right)^2} \tag{24}$$

where σ_{P} is the counting uncertainty of the output pulse and σ_{T} is the timing uncertainty of the timing system.

When σ_{P} = 1 and σ_{T} = 10^{-6} s, the combined standard measurement equals $\sigma_{\bar{\dot{\alpha}}}(i,j) \approx 3.84\times10^{-4}/\ T_{\mathrm{m}}\ (i,j)$. Thus, to ensure that the measurement uncertainty of PIGA is less than 1×10^{-6} rad/s, the test time must be longer than 384 s. Then, the calibration uncertainty could be estimated according to Eq.(22) and calculation results of $RES(n)$. In order to analyze the influence of the different numbers of positions on the calibration uncertainty, the simulations of

integer periodic vibration method[22] for PIGA testing on the linear vibration are constructed. The simulation parameters of PIGA are set as follows: k_0 =1.5×10^{-4}rad·s^{-1}, k_z = 0.56 (rad·s^{-1})/g, k_{zz} =6.0×10^{-6} (rad·s^{-1})/g^2, k_y=5.0×10^{-6} (rad·s^{-1})/g^2, and k_3 =7×10^{-7} (rad·s^{-1})/g^3.

The uncertainty estimation results of the nonlinear error coefficients for different numbers of the test positions {6-position (θ_{vi}=π(i-1)/3, $i=1,2,\cdots,6$), 9-position (θ_{vi}= 2π(i-1)/9, $i=1,2,\cdots,9$), 10-position (θ_{vi}= π(i-1)/5, $i=1,2,\cdots,10$), and 22-position (θ_{vi} = π(i-1)/12, $i=1,2,\cdots,24; i\neq 7,19$)} and different vibration frequencies (5Hz, 7Hz, and 10Hz) are shown in Fig.8.

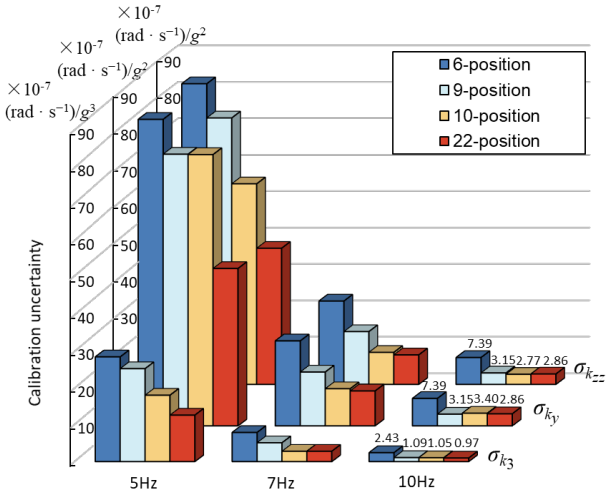

Fig. 8 Calibration uncertainty of nonlinear error coefficients for different numbers of test positions and different vibration frequencies.

Obviously, the nonlinear error terms of PIGA cannot be fully excited in the lower vibration frequency test. The magnitudes of calibration uncertainties are more than 10^{-6} rad/s/g^2 when f_v = 5 Hz and f_v = 7 Hz. In addition, it is shown that the calibration uncertainties of the second-order nonlinear coefficients for the 6-position calibration test are more than 7×10^{-7} rad/s/g^2 which are much higher than those for the other three multi-position calibration tests. It is verified that the number of test positions can significantly affect the calibration uncertainty of nonlinear coefficients when $n \leq 10$. Moreover, the calibration uncertainty of k_y in 9-position test is higher than that in 10-position test. It is indicated that the calibration pose of PIGA will also affect the calibration uncertainty. With the increase of the number of test positions, the calibration uncertainties only slightly increase in the 22-position test. Thus, the number of the test positions should be reasonably designed to match the calibration uncertainty and cost requirements.

5.1.4. Parameter design, PIGA installation, and alignment

Based on the above analyses and error calibration model of PIGA, the test positions, time, and vibration frequencies should be reasonably set before the calibration test. Specifically, the number of the precession period should be designed to ensure that t_2 (in Fig.4) is kept as short as possible.

PIGA is installed on the indexing head while ensuring that the table top's static balance is corrected. According to the error calibration model of PIGA, the installation errors may also affect the calibration uncertainty. Thus, PIGA must be aligned before the test. The common alignment method calculates the misalignment angle by PIGA itself in 2-position test (θ_{vi} = 0° and 180°). Since the input accelerations are too small to excite the nonlinear error terms of PIGA, the alignment model of PIGA can be expressed as follows:

$$\ddot{\alpha}+\omega_{ie}\sin\left(\lambda-\theta_{vi}\right)=k_0+k_z\cos\left(\theta_{vi}+\Delta\theta_h\right) \tag{25}$$

where $\Delta\theta_h$ is the misalignment angle.

Then, the misalignment angle can be approximately calculated as follows:

$$\Delta\theta_h=\arccos\left(\frac{\bar{\dot{\alpha}}_0-\bar{\dot{\alpha}}_{180}+2\omega_{ie}\sin\lambda}{2k_z}\right) \tag{26}$$

where the value of k_z can be obtained via the gravity field test.

When $\sigma_{\bar{\dot{\alpha}}}$ is equal to 6.8×10^{-6} rad/s, the measurement uncertainty of latitude is 0.1°. Moreover, the calibration uncertainty of k_z is 1×10^{-4} (rad·s^{-1})/g, and the propagation of the measurement uncertainty of $\Delta\theta_h$ is expressed as

$$\sigma_{\Delta\theta_h}=\sqrt{2\left(\frac{\partial\Delta\theta_h}{\partial\bar{\bar{\alpha}}}\sigma_{\bar{\bar{\alpha}}}\right)^2+\left(\frac{\partial\Delta\theta_h}{\partial\lambda}\sigma_\lambda\right)^2+\left(\frac{\partial\Delta\theta_h}{\partial k_z}\sigma_{k_z}\right)^2}\approx 8.6\times10^{-6}\,\text{rad} \tag{27}$$

Thus, the acceleration errors caused by $\Delta\theta_h$ may be less than 8.6×10^{-5} g and the corresponding error terms in the error calibration model of PIGA can be assumed as negligible.

5.2. PIGA test

After planning and preparation, the calibration test should be started in different positions in sequence. According to Eq.(19), the PIGA testing comprises two parts:

(1) Linear Vibration Test: When the linear vibration table is running stably, the control & monitoring system starts to monitor the running status. Then, the zero time and t_1 values are recorded. Parameter T_m is recorded once the number of the output pulses reaches the preset value. Once the read head moves to the zero position for the next time, t_2 and N_p are recorded.

(2) Static Test: The static test is designed after vibration test in the same position to compensate for the installation errors such as $\Delta\theta_{xv0}$ and $\Delta\theta_{xv2}$. The test process is similar to the linear vibration test. However, the linear vibration table should remain static state. The test time should also ensure that PIGA precesses within integer periods. Then, once the PIGA test is completed, the corresponding data should be acquired.

5.3. Coefficient identification

Once the PIGA has been tested for all positions and vibration frequencies in the designed order, the nonlinear error coefficients can be identified based on LS method. Then, the residuals and the standard deviations of residual are calculated via Eq.(21). According to Ref.24, the statistical analysis was conducted to evaluate the test reliability:

$$\begin{cases}\mu=\max|\boldsymbol{e}|/\sigma\\ \mu_c=1.25+\ln\sqrt{N/3}\end{cases} \tag{28}$$

where N is the number of the test points.

If $\mu\geq\mu_c$, the test data may have a breaking point. If $\mu<\mu_c$, the test data could be accepted. Then, the calibration uncertainty of the nonlinear coefficients of PIGA can be calculated by Eq.(22) to determine whether they meet the requirements of the calibration uncertainty. In order to evaluate the calibration uncertainty with respect to the input acceleration, the proportional residual error is designed as follows:

$$e_{a(i,j)}=\left|e_{(i,j)}/a_{\text{nominal}}(i,j)\right| \tag{29}$$

where $e_{(i,j)}$ is the residual error and $a_{\text{nominal}}(i,j)$ is the nominal amplitude of the input acceleration of linear vibration table.

6. Experiments and simulations

Based on the error calibration model of PIGA and the calibration test process, the main error sources should be firstly measured and compensated for the error calibration model.

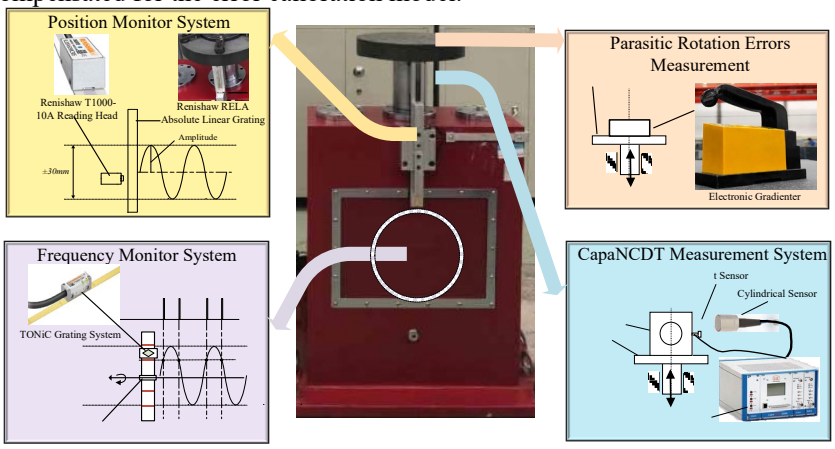

Fig. 9 Overall measurement experimental diagram of main error sources.

6.1. Error measurement experiments

The error measurement experiments are conducted, including parasitic translation errors experiment, frequency stability experiment, parasitic rotation errors experiment, and lateral acceleration experiment, as shown in Fig.9, which utilize position monitor system, frequency monitor system, electronic gradienter, and CapaNCDT measurement system respectively. The detailed parameters of linear vibration table, measurement systems, and PIGA are summarized as shown in Table 4.

Table 4 Detailed parameters of experimental system.

System	Parameter	Performance	System	Parameter	Performance
Linear Vibration Table	Top Table Size	Φ=300 mm	Position Monitor System	Measurement Accuracy	< ±1 μm
	Payload Size	200 mm×200 mm ×220 mm		Resolution	< 2 nm
	Useful Load	10 kg	Frequency Monitor System (TONiC Grating System)	Measurement Accuracy	< ±1 μm
	Frequency Range	0.1-10 Hz		Low Signal Output Jitter	<±0.5 nm RMS
	Frequency Stability	$<5.0\times10^{-4}$		Sub-Divisional Error (SDE)	<±30 nm
	Working Amplitude	±30 mm		Resolution	< 2 nm
	Acceleration Amplitude	0.1 *G*-10 *G*	Electronic Gradienter	Measurement Accuracy	< 0.01″
	Waveform Distortion	$<1.7\times10^{-3}$	CapaNCDT Measurement System	Measuring Range	1 mm
	Lateral Acceleration	<0.1 *g*		Resolution	0.75 nm (static, 2Hz) 20 nm (dynamic, 8.5 kHz)
	Magnetic Field Intensity	<0.5 Gs		Linearity	±0.05 FSO

PIGA					
Parameter	Performance	Parameter	Performance	Parameter	Performance
Synchronization Accuracy	<100 μs	Measurement range	$\geq10^{-6}$ *g* – 20 *g*	Output Pulse	16384 per period
Timing Accuracy	<100 μs	Angle Measurement Error	<1.5′	Pulse Counting Error	<±2 per period

6.1.1. Parasitic translation errors experiment

The position monitor system is composed of absolute grating ruler, reading head, and grating interface circuit which are all mounted in the linear vibration table. The absolute grating ruler is high-precision invar steel RELA absolute linear grating of which the precision is less than ±1 μm. The signal sampling frequency of the grating interface is 5000 Hz. The harmonic components of $D_z(t)$ can be calculated by the Fast Fourier Transform (FFT) algorithm as shown in Table 5. The amplitude of displacement can be expressed as follows:

$$D_z(t)=A_s+(Z_{s1}+A_0)\sin(\omega_v t+\gamma_0)+Z_{c1}\cos(\omega_v t+\gamma_0)+\sum_{j=2}^{\infty}\left(Z_{sj}\sin(j\omega_v t+\gamma_0)+Z_{cj}\cos(j\omega_v t+\gamma_0)\right) \quad (30)$$

where A_s is the average value of the measured displacement and γ_0 is the initial phase.

Taking the highest frequency of 10 Hz as an example, the measurement error of the maximum vibration amplitude caused by sampling delay can be calculated by

$$\Delta A_{max}=A_0\sin(\frac{\pi}{2})-A_0\sin(\frac{\pi}{2}+2\pi\times\frac{10}{5000})=2.37\times10^{-6}\,\mathrm{m} \quad (31)$$

The other values of ΔA_{max} for different frequencies are estimated as shown in Table 5. Compared with the values of parasitic translation errors in Table 5, the values of ΔA_{max} are close to the second-order harmonic coefficients and much smaller than the value of Z_{s1}. According to Eq. (19), the maximum values of the output errors caused by sampling delay are all less than 7×10^{-8} rad/s. Generally, the output uncertainty of PIGA is about 1×10^{-7} rad/s. Thus, the measurement error caused by sampling delay cannot affect the calibration of high-order error coefficients of PIGA.

It is illustrated that the value of Z_{s1} increases with the vibration frequency within the range from −88 μm to 83 μm. Then, the error accelerations caused by Z_{s1} could be higher than $1.80\times10^{-6}g$ when the vibration frequency is 10Hz. Based on the measurement results, Z_{s1} can be obtained as follows:

$$Z_{s1}(j)=-0.1299+0.0032\omega_{vj} \quad (32)$$

The error calibration model should be compensated with Eq.(32) to identify the nonlinear error coefficients of PIGA.

Table 5 Measurement results of parasitic translation in vertical direction.

Frequency (Hz)	Z_{s1} (mm)	ΔA_{max} (mm)	Z_{s2} (mm)	Z_{c2} (mm)
1	−0.0886	2.37×10^{-5}	0.0024	−0.0042
3	−0.0774	0.0002	0.0004	−0.0207
5	−0.0548	0.0006	−0.0030	0.0043
7	−0.0048	0.0012	−0.0019	−0.0141
9	0.0504	0.0019	−0.0014	0.0475
10	0.0834	0.0024	0.0021	−0.0024

6.1.2. Frequency stability experiment

The TONiC grating system is utilized in the measurement system. It is regarded as a new generation of ultra-compact linear grating, which is specially designed for high-dynamic-precision linear motion systems and providing higher accuracy. TONiC grating system consists of an incremental grating ruler, a reading head and a grating interface circuit board as shown in Fig.9. In order to measure the frequency stability, the linear vibration table should vibrate at the nominal frequency from 0.1 Hz to 10 Hz. After the vibration is stable, the measurement frequency f_e is recorded continuously over 10 periods (e=1,2,3,... ,10). Then, the vibration frequency stability can be calculated by $\sigma_f/f=\frac{1}{3\overline{f}}\sqrt{\sum_{e=1}^{10}\left(f_e-\overline{f}\right)^2}$, where $\overline{f}$ is the average value of f_e. The measurement results of $\overline{f}$ and the average frequency errors Δf_v ($\Delta f_v=f-\overline{f}$) are given in Table 6. It is verified that the accuracy of frequency can be ensured because the maximum value of Δf_v and σ_f/f are less than 5.0×10^{-6} Hz and 2.0×10^{-5}, respectively, which are far less than the specified value in Table 4.

Then, the average precession angular velocity error of PIGA caused by the vibration frequency error can be approximately estimated as

$$\begin{aligned}\Delta\overline{\alpha}_i&=f_i\int_0^{10/f_i}\left(4\pi^2k_zA_0\left(f_i+3\sigma_f\right)^2\sin2\pi\left(f_i+3\sigma_f\right)t\right)\mathrm{d}t/10\\&=A_0 2\pi f_i\left(f_i+3\sigma_f\right)\left(\left(\cos20\pi\left(\left(f_i+3\sigma_f\right)/f_i\right)-1\right)\right)k_z/10\end{aligned}\tag{33}$$

The maximum value of $\Delta\overline{\alpha}_i$ is less than -3.4×10^{-11} rad/s as shown in Table 6. It is illustrated that the frequency stability of the linear vibration table can meet the requirement of test accuracy for calibrating PIGA.

Table 6 Measurement results of vibration frequency stability

Frequency (Hz)	0.1	1	2	3	4	5	6	7	8	9	10
$\overline{f}$	0.1000013	1.0000005	1.999999	3.000001	4.000003	4.9999973	6.000004	6.9999978	8.0000013	8.9999971	10.000040
Δf_v (Hz)	-1.3×10^{-6}	-5.0×10^{-7}	1.0×10^{-7}	-1.0×10^{-7}	-3.0×10^{-6}	2.7×10^{-6}	-4.0×10^{-6}	2.2×10^{-6}	-1.3×10^{-6}	2.9×10^{-6}	4.0×10^{-6}
σ_f/f	1.8×10^{-5}	3.5×10^{-6}	4.0×10^{-6}	6.0×10^{-6}	5.5×10^{-6}	7.4×10^{-6}	9.0×10^{-6}	7.5×10^{-6}	1.0×10^{-5}	9.6×10^{-6}	1.8×10^{-5}
$\Delta\overline{\alpha}_e$ (rad/s)	-3.4×10^{-11}	-2.4×10^{-14}	-1.8×10^{-14}	-4.0×10^{-14}	-2.3×10^{-14}	-3.9×10^{-14}	-6.6×10^{-14}	-3.4×10^{-14}	-7.2×10^{-14}	-5.5×10^{-14}	-3.1×10^{-13}

6.1.3. Parasitic rotation errors experiment

According to Eq.(17), the parasitic rotation error terms a_{xs1} will also affect the calibration uncertainty. Thus, the magnitude of parasitic rotation errors should be estimated by unitizing the electronic gradienter (the equivalent accuracy of position is less than 0.01″ and the equivalent resolution is 0.005″). When the angular positions of the crank disk are 0°, 60°, 120°, 180°, 240°, or 300°, the indication outputs of gradienter along the three axis lines ϕ_x, ϕ_y, ϕ_z are shown in Table 7.

The harmonic components of $\Delta\alpha_x(t)$ can be obtained as follows:

$$\begin{cases}a_{xs1}=\dfrac{2}{12}\displaystyle\sum_{i=0}^{11}\left[\phi_x\left(\frac{2\pi i}{12}\right)\sin\frac{2\pi i}{12}\right]\\ a_{xc1}=\dfrac{2}{12}\displaystyle\sum_{i=0}^{11}\left[\phi_x\left(\frac{2\pi i}{12}\right)\cos\frac{2\pi i}{12}\right]\end{cases}.\tag{34}$$

Similarly, the harmonic components of $\Delta a_y(t)$ and $\Delta a_z(t)$ can also be calculated by Fourier transforms. The calculated results are shown as follows: $a_{xs1} = -0.92''$, $a_{xc1} = 0.19''$, $a_{ys1} = -0.46''$, $a_{yc1} = -1.49''$, $a_{zs1} = 0.16''$, and $a_{zc1} = 0.16''$. According to the conducted error analysis in Section 5, error accelerations caused by the parasitic rotation errors are 5×10^{-5} g, 7.5×10^{-5} g, and 7.5×10^{-5} g, respectively. Thus, the corresponding influence of $\Delta a_y(t)$ and $\Delta a_z(t)$ on the identification of nonlinear coefficients can be assumed as negligible. Therefore, the error calibration model defined by Eq.(20) should be compensated with the measurement value of a_{xs1}.

Table 7 Measurement results of parasitic rotation errors

Angle position	ϕ_x ($''$)	ϕ_y ($''$)	ϕ_z ($''$)
0°	15.7	0.15	10.08
60°	16.6	−1.725	10.09
120°	16.725	−1.20	9.74
180°	17.8	0.90	10.45
240°	16.925	1.50	10.03
300°	15.725	0.75	10.23

6.1.4. Lateral acceleration experiment

Based on the kinetic analysis of the linear vibration table, we can find that the main error component during the PIGA testing caused by resonance is lateral acceleration. The lateral acceleration can be calculated by using the capacitive Non-Contact Displacement Transducer (CapaNCDT) system, as shown in Fig.9. When the working frequency is 10 Hz, the parasitic translation $\Delta x(t)$ in the horizontal plane can be measured, and the maximum value of $\Delta x(t)$ is less than 0.006 mm.[22] Thus, the maximum amplitude of lateral acceleration $a_{\text{O-max}}$ has been restrained to be less than 2.4×10^{-3} g. Then, the value of $\bar{\alpha}_{\text{la}} = 0.5k_x a_{\text{O-max}}{}^2$ is less than 5.8×10^{-11} rad/s when k_x is approximately equal to 1×10^{-5} rad/s/g^2. Obviously, the lateral acceleration caused by resonance cannot affect the calibration accuracy of PIGA. Therefore, as long as we ensure that the lateral acceleration is less than 2.4×10^{-3} g during the calibration testing, the resonance influence could be ignored.

6.2. PIGA calibrations

6.2.1. Design of integral precession calibration method

Based on the results of the error measurement experiment, the simulations are constructed to verify the applicability and effectiveness of the proposed calibration method. The clock frequency of the CPU in the measurement system is set to 2.9 GHz, the period is 340 ps, and the timing resolution is 50 ns to measure the relative test time precisely. Thus, the timing uncertainty can reach 10^{-7}s.

It is assumed that the local latitude is 39.94°. Taking $\theta_{vi} = 0°$ and 180° as examples, the time parameters of PIGA calibration are constructed for different vibration frequencies as shown in Table 8. It should be noted that the test time of different vibration frequencies are relatively close to the static test because the magnitudes of the nonlinear error terms of PIGA are much smaller than those of the other linear accelerometers in the sinusoidal vibration test. Thus, the timing uncertainty should significantly affect the output accuracy of PIGA.

Table 8 Time parameters of integral precession calibration.

Parameter \ f_v	8 Hz	9 Hz	10Hz
$N_{p(0,j)}$	4485	5042	5602
$t_{1(0,j)}$ (s)	0.009945	0.009466	0.0107632
$T_{m(0,j)}$ (s)	560.532589	560.165550	560.133591
$t_{2(0,j)}$ (s)	0.102357	0.066135	0.0771802
$T_{m(0,0)}$ (s)	560.842523	560.845114	560.850239
$N_{p(\pi,j)}$	4490	5053	5613
$t_{1(\pi,j)}$ (s)	0.010760	0.010706	0.0097032
$T_{m(\pi,j)}$ (s)	561.244595	561.352932	561.285019
$t_{2(\pi,j)}$ (s)	0.016166	0.102216	0.024692
$T_{m(\pi,0)}$ (s)	561.149292	561.153358	561.162066

6.2.2. Comparison of integer periodic vibration method

Furthermore, a comparison of the integer periodic vibration method is performed to verify the superiority of the proposed method. According to Eq.(17), the calibration error model of the integer periodic vibration method can be deduced as

$$\bar{\dot{\alpha}}_{\mathrm{v}}(i,j)-\bar{\dot{\alpha}}_{\mathrm{v}}(i,0)=\frac{1}{2}a_{\mathrm{xs1}}k_z A_j/g\sin\theta_{vi}+\frac{1}{2}\left(1-\frac{2Z_{\mathrm{s1}}}{A_0}\right)k_{zz}A_j{}^2/g^2\cos^2\theta_{vi}+\frac{1}{2}\left(1-\frac{2Z_{\mathrm{s1}}}{A_0}\right)k_2'A_j{}^2/g^2\sin^2\theta_{vi}+\frac{3}{2}k_3A_j{}^2/g^2\cos^3\theta_{vi} \tag{35}$$

Thus, the nonlinear error coefficients of PIGA can be identified by LS method. The number of vibration periods should be the same as shown in Table 8, and the vibration time of the integer periodic vibration calibration $T_{\mathrm{V}(i,j)}$ is set as shown in Table 9. It is noted that the testing time of the two calibration methods are almost the same, which means that the test cost and efficiency will not significantly increase.

Table 9 Time parameters of integer periodic vibration calibration

Parameter \ f_{v}	8 Hz	9 Hz	10Hz
$T_{V(0,j)}$ (s)	560.625000	560.222222	560.200000
$T_{V(\pi,j)}$ (s)	561.250000	561.4444444	561.300000

6.2.3. Calibration results

The calibration results of integral precession calibration and integer periodic vibration calibration are shown in Table 10. It is shown that the calibration uncertainties significantly decrease with the increase of f_{v} since the higher input acceleration can excite nonlinear error terms more adequately. Meanwhile, compared with the simulation results of integer periodic vibration method, the proposed calibration method can calibrate main nonlinear error coefficients more accurately. The magnitude of absolute error $\Delta\hat{k}_{zz}$ decreases from 10^{-6} rad/s/g^2 to 10^{-7} rad/s/g^2. In addition, the magnitude of $\Delta\hat{k}_3$ decreases from 10^{-7} rad/s/$g^3$to 10^{-8} rad/s/g^3.

Table 10 Simulation calibration results of error coefficients

Coefficient \ f_{v}		8 Hz	9 Hz	10Hz
Proposed method	k_{zz} (rad/s/g^2)	6.13×10^{-6}	5.90×10^{-6}	6.02×10^{-6}
	Δk_{zz} (rad/s/g^2)	1.26×10^{-7}	1.05×10^{-7}	1.56×10^{-8}
	k_3 (rad/s/g^3)	7.09×10^{-7}	6.70×10^{-7}	6.98×10^{-7}
	Δk_3 (rad/s/g^3)	9.19×10^{-9}	7.02×10^{-8}	2.49×10^{-9}
Integer periodic vibration method	k_{zz} (rad/s/g^2)	6.87×10^{-6}	9.05×10^{-6}	5.82×10^{-6}
	Δk_{zz} (rad/s/g^2)	8.68×10^{-7}	3.05×10^{-6}	1.86×10^{-7}
	k_3 (rad/s/g^3)	1.25×10^{-6}	1.65×10^{-6}	1.33×10^{-6}
	Δk_3 (rad/s/g^3)	5.47×10^{-7}	9.53×10^{-7}	6.32×10^{-7}

Furthermore, the calibration results for different test positions by utilizing the proposed method are given in Table 11 when the vibration frequency is 10 Hz. The absolute errors of second error coefficients are all less than 10^{-7} rad/s/g^2, and their values decrease with the increase of the number of test positions. Meanwhile, according to the calculation results of the sensitivity analysis in Section 5, standard deviations are significantly decreased. Consequently, the calibration uncertainty is decreased by over 50%. It is also shown that the absolute error and the calibration uncertainty significantly increase without compensating for the parasitic translation errors and parasitic rotation errors for PIGA calibration. Thus, it is necessary to accurately measure and compensate for these errors.

In order to further verify the effectiveness of the proposed method, the integer periodic precession method for multi-frequency test[21] and the integer periodic vibration method for 9-position test[22] are applied. The multi-frequency calibration method is often used to calibrate the second-order coefficients by upward and downward testing with PIGA mounted vertically, and then the cross-quadratic term coefficient can be calibrated by inclined position testing (θ_{vi} = 45°). Thus, the multi-frequency calibration test is conducted at 3 angular positions (θ_{vi} = 0°, 45°, and 180°), and each position is tested for 3 frequencies (8, 9, and 10 Hz).

Table 11 Calibration results of multi-position and classical methods

Multi-position	Calibration results			Absolute error				Calibration uncertainty		
	k_{zz} (rad/s/g^2)	k_{y} (rad/s/g^2)	k_3 (rad/s/g^3)	Δk_{zz} (rad/s/g^2)	Δk_{y} (rad/s/g^2)	Δk_3 (rad/s/g^3)	Standard Deviation (rad/s)	$\sigma_{k_{zz}}$	$\sigma_{k_{\mathrm{y}}}$	σ_{k_3}

								(rad/s/g^2)	(rad/s/g^2)	(rad/s/g^3)
6	6.04×10^{-6}	4.92×10^{-6}	6.13×10^{-7}	3.6×10^{-8}	8.2×10^{-8}	8.7×10^{-8}	8.9×10^{-6}	8.7×10^{-8}	8.6×10^{-8}	5.1×10^{-8}
9	5.96×10^{-6}	5.04×10^{-6}	7.30×10^{-7}	3.6×10^{-8}	3.9×10^{-8}	3.0×10^{-8}	7.4×10^{-6}	7.4×10^{-8}	5.9×10^{-8}	3.4×10^{-8}
10	5.99×10^{-6}	5.05×10^{-6}	7.33×10^{-7}	6.0×10^{-9}	4.5×10^{-8}	3.3×10^{-8}	4.4×10^{-6}	3.5×10^{-8}	3.3×10^{-8}	2.0×10^{-8}
10 (a_{xs1} =5×10^{-6} rad)	5.96×10^{-6}	5.06×10^{-6}	6.42×10^{-7}	4.4×10^{-8}	5.8×10^{-8}	5.8×10^{-8}	8.5×10^{-6}	6.9×10^{-8}	6.4×10^{-8}	4.0×10^{-8}
10 (Z_{s1} =0.0834 mm)	5.89×10^{-6}	5.09×10^{-6}	6.72×10^{-7}	1.0×10^{-7}	9.1×10^{-8}	2.8×10^{-8}	6.2×10^{-6}	4.7×10^{-8}	4.7×10^{-8}	2.3×10^{-8}
Integer periodic Precession method for multi-frequency	6.12×10^{-6}	5.12×10^{-6}	1.20×10^{-6}	1.2×10^{-7}	1.2×10^{-7}	5.0×10^{-7}	1.7×10^{-5}	1.4×10^{-7}	1.3×10^{-7}	7.6×10^{-7}
Integer periodic vibration method for 9-position	6.20×10^{-6}	5.15×10^{-6}	7.95×10^{-7}	2.0×10^{-7}	1.5×10^{-7}	9.5×10^{-8}	3.99×10^{-5}	4.3×10^{-7}	4.3×10^{-7}	1.5×10^{-7}

The calibration results of the two compared methods are shown in Table 11. It is shown that the standard deviations of the compared calibration methods are all more than 1×10^{-5} rad/s, but the order of the standard deviation of the proposed calibration methods for 9-position testing is 10^{-6} rad/s. Similarly, the order of absolute error and calibration uncertainty of the second-order term coefficients are decreased from 10^{-7} rad/s/g^2 to 10^{-8} rad/s/g^2 by utilizing the proposed method. It is verified that the proposed method can precisely and efficiently calibrate the nonlinear error coefficients of PIGA. Compared with the other two multi-position calibration method based on D-optimal design, the order of absolute error of k_3 increases from 10^{-8} rad/s/g^3 to 10^{-7} rad/s/g^3, and the calibration uncertainty of k_3 increases by more than five times by using the integer periodic precession method for multi-frequency test. In addition, the absolute errors of integer periodic precession method are obviously less than those of the integer periodic vibration method. It is illustrated that the calibration accuracy of the nonlinear error term coefficients can be significantly improved by compensating for the error terms generated by linear vibration without integer periods.

6.3. Calibration result evaluation

Residual errors for different test positions are restrained within $\pm8\times10^{-6}$ rad/s, while the residual errors of the 10-position test are smaller than those of the 6-position test as shown in Fig.10 (a). It is also verified that additional test positions can significantly improve the calibration uncertainty of the nonlinear error coefficients of PIGA. In addition, the residual error distribution illustrates that no apparent systematic errors exist in the error calibration model and that the proposed calibration method can meet the adequacy of model equations.

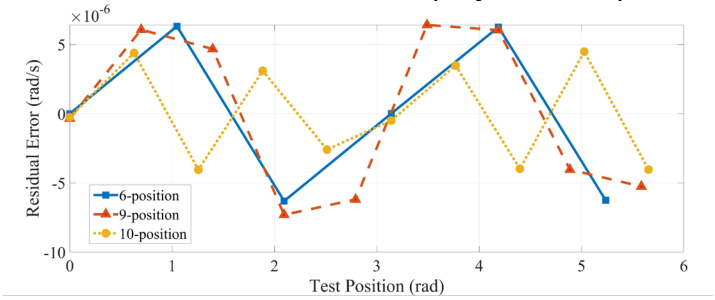

(a) Residual errors of different numbers of test positions.

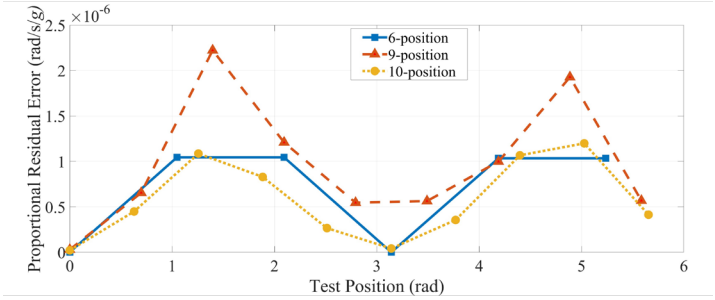

(b) Proportional residual errors of different numbers of test positions.

Fig. 10 Calibration result evaluation of proposed methods for different numbers of test positions.

According to Eq.(27), the reliability of the multi-position test can be calculated as follows: ($\mu_6 = 0.7105$) < ($\mu_{c6} = 1.5964$), ($\mu_9 = 0.9908$) < ($\mu_{c9} = 1.7993$), ($\mu_{10} = 1.0153$) < ($\mu_{c10} = 1.8516$). In other words, the test data can be accepted to identify the nonlinear error coefficients of PIGA.

Proportional residual errors of the three multi-position tests are shown in Fig.10 (b). The distribution of the proportional residual errors for different tests is sinusoidal due to the cosine input accelerations $A_j\cos\theta_{vi}$. Moreover, although the standard deviation of the 9-position test is smaller than that of the 6-position test, the proportional residual errors of the 9-position test are more than double the value of that of the 6-position test and the 10-position test. It is indicated that, since the smaller input acceleration cannot fully excite the nonlinear error terms of PIGA, the test positions of PIGA should be reasonably designed to avoid the test points that are close to the angle position $\theta_{vi} = 90°$ and $\theta_{vi} = 270°$.

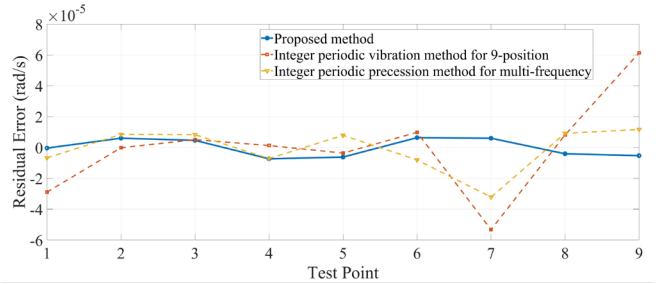

(a) Residual errors of different calibration methods

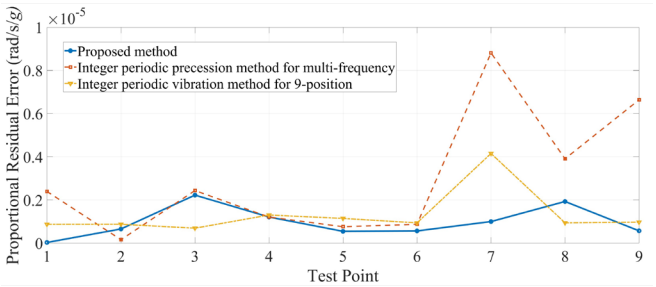

(b) Proportional residual errors of different calibration methods

Fig. 11 Calibration result evaluation of different calibration methods.

The residual errors for different calibration methods are shown in Fig.11 (a). Compared with the two classical calibration methods, the residual errors are much smaller by using the proposed calibration method. Obviously, a low residual generally signifies that the model is proficient at delineating the distributional characteristics of the test data. It is verified that the proposed error calibration model has a higher applicability for the multi-position vibration test. The proportional residual errors of the different calibration methods are shown in Fig.11 (b). The proportional residuals of the last three test points by using the integer periodic vibration method for 9-position testing are more than 4.0×10^{-6} rad/s/g, which are much larger than those of the other two calibration methods. It is demonstrated that the common error calibration model is not suitable for high-precise calibration testing of PIGA without compensating for the error terms of nonintegral vibration. In addition, the distribution of proportional residuals is concentrated within 2.2×10^{-6} rad/s/g by using the proposed method. It is verified that the proposed D-optimal multi-position mode could be more effectiveness.

4. Conclusions

In this paper, the integral precession calibration method was proposed to calibrate the nonlinear error coefficients of the pendulous integrating gyroscopic accelerometer (PIGA). According to the established corresponding coordinate systems, the precise inputs about the three referent axes of PIGA were deduced and the error calibration model of PIGA precession within integer periods was established. The main errors of the measurement systems could be avoided, and the designed calibration process could suppress the output interference of PIGA; hence, the measurement uncertainty and the calibration efficiency of PIGA were further improved. According to the conducted analysis, experimental investigation, and simulation results, the following conclusions can be drawn:

(1) Compared with the integer periodic vibration method, the proposed integral precession calibration method

can more accurately identify the nonlinear error coefficients of PIGA. More specially, the calibration uncertainty of k_3 could be approximately decreased to one-tenth of the value.

(2) The optimization and design of the complete calibration process can further improve the calibration uncertainty and test efficiency. According to the verification results, the calibration uncertainties were reduced by about 50% using the 10-position calibration test.

(3) By comparing the calibration test without parameter optimization, without compensating for the parasitic errors, and the other two classical calibration method, it was observed that the proposed method could significantly reduce the influence of the errors caused by the test instruments and the PIGA output unit.

Consequently, the proposed calibration method and the designed calibration process can significantly improve the calibration uncertainty of PIGA. In addition, the proposed method can be applied for enhancing the high-g performance of high-precision inertial instruments. Further work will be conducted using this calibration method for sensor array and the online calibration method can be investigated by upgrading the calibration system and identification algorithm.

References

1. Yue L, Zhou H, Duan R. Fault diagnosis of remainders inside PIGA based on pattern recognition algorithm. *Proceedings of the 2020 international conference on pattern recognition and intelligent systems*. New York: ACM, 2020:1–5.[LinkOut]
2. Gomathi K, Sakthivel R, Joseph John Marshal S, et al. Design, fabrication, and performance analysis of intelligent mesoscale capacitive accelerometer for vibration measurement. *J Test Eval* 2021;**49**(4):20200176.[LinkOut]
3. Cocconcelli F, Mora N, Matrella G, et al. High-accuracy, unsupervised annotation of seismocardiogram traces for heart rate monitoring. *IEEE Trans Instrum Meas* 2020;**69**(9):6372–80.[LinkOut]
4. Kokuyama W, Shimoda T, Nozato H. Primary accelerometer calibration with two-axis automatic positioning stage. *Measurement* 2022;**204**: 112044.[LinkOut]
5. Hajiyev C, Cilden-Guler D. Attitude and gyro bias estimation by SVD-aided EKF. *Measurement* 2022;**205**: 112209.[LinkOut]
6. Zhang MQ, Yan ST, Deng ZG, et al. Cross-coupling coefficient estimation of a nano-g accelerometer by continuous rotation modulation on a tilted rate table. *IEEE Trans Instrum Meas* 2021;**70**: 1–12.[LinkOut]
7. Sohrabi H, Ebadollahi S. Accuracy enhancement of MEMS accelerometer by determining its nonlinear coefficients using centrifuge test. *Measurement* 2017;**112**: 29–37.[LinkOut]
8. Wang SM, Ren SQ. Calibration of cross quadratic term of gyro accelerometer on centrifuge and error analysis. *Aerosp Sci Technol* 2015;**43**: 30–6.[LinkOut]
9. Dong XS, Huang XL, Du GZ, et al. Calibration method of accelerometer based on rotation principle using double turntable centrifuge. *Micromachines* 2021;**13**(1):62.[LinkOut]
10. Wang SM, Ren SQ. Calibration accuracy of error model coefficients K_2 and K_3 of gyro accelerometer influenced by errors of centrifuge. *Nanotechnol Precis Eng* 2013;**11**(2):140–5 [Chinese].
11. Sun YB, Ren SQ, Wang CH. Calibration method of quartz accelerometer on dynamic centrifuge. *Chin J Aeronaut* 2022;**35**(6):262–72.[LinkOut]
12. Ripper GP, Dias RS, Garcia GA. Primary accelerometer calibration problems due to vibration exciters. *Measurement* 2009;**42**(9):1363–9.[LinkOut]
13. Badri AE, Sinha JK, Albarbar A. A typical filter design to improve the measured signals from MEMS accelerometer. *Measurement* 2010;**43**(10):1425–30.[LinkOut]
14. Zou ZX, Zeng M, Zhang X, et al. Study on calibration algorithms of gyroscopic drift error that affected by the acceleration harmonic errors of vibration table. *2017 IEEE international instrumentation and measurement technology conference (I2MTC)*. Piscataway: IEEE Press; 2017.p.1–6.[LinkOut]
15. Yu P, Yan L, Zhang J, et al. Research on error suppression technology of PIGA under vibration condition. *Noise Vib Control* 2019; 39(2):37-41.
16. Dong XM, Xiong L, Guan W, et al. Analysis of the combined acceleration model reproduced by centrifuge-vibrator system. *J Test Meas Technol* 2014;**28**(3):214–8 [Chinese].
17. Wei Y, Yang JH, Li PF, et al. Analysis and optimization method of the vibration rectification error of a pendulous accelerometer. *IEEE Sens J* 2021;**21**(18):19847–56.[LinkOut]
18. Guan W, Tang L. Simulation of testing transverse sensitivity of inertial accelerometer with vibration table. *Aerospace Control* 2018; 36(5):19-24.

19. Chen X, Sun F, Li Q, et al. High order error coefficient identification of quartz flexible accelerometer based on multi-direction vibration test. *Transducer and Microsystem Technology* 2016; 35(11):51-3,57.
20. Yue TY, Pan X, Yang YQ, et al. A new method to improve the navigation performance of SINS in vibration environment. *IEEE Sens J* 2021;**21**(1):438–46.[LinkOut]
21. He D, Yan X, Zhu J, et al. Method of quadratic term coefficient separation of pendulous integrating gyro-accelerometer on linear vibrator. *Transducer and Microsystem Technology* 2020; 39(10):24-6,30.
22. Ren SQ, Sun C. A new method for calibrating nonlinear coefficients of PIGA on linear vibrator. *IEEE Trans Instrum Meas* 2019;**68**(8):2898–906.[LinkOut]
23. Ren SQ, Liu QB, Zeng M, et al. Calibration method of accelerometer's high-order error model coefficients on precision centrifuge. *IEEE Trans Instrum Meas* 2020;**69**(5):2277–86.[LinkOut]
24. IEEE recommended practice for precision centrifuge testing of linear accelerometers. *IEEE Std 836 1991* 1992:1–80.[LinkOut]